

**ELECTROTHERMAL ANALYSIS OF
INTEGRATED CIRCUITS:
A REALIZATION BY INFRARED THERMOGRAPHY**

by

Farnoos Farrokhi

BASc., Ferdowsi University

Mashhad, Iran

September 2003

A thesis

presented to Ryerson University

in partial fulfillment of the

requirement for the degree of

Master of Applied Science

in the program of

Electrical and Computer Engineering.

Toronto, Ontario, Canada 2009

© Farnoos Farrokhi 2009

Author's Declaration

I hereby declare that I am the sole author of this thesis.

I authorize Ryerson University to lend this thesis to other institutions or individuals for the purpose of scholarly research.

Signature

A rectangular box containing a redacted signature.

I further authorize Ryerson University to reproduce this thesis by photocopying or by other means, in total or in part, at the request of other institutions or individuals for the purpose of scholarly research.

Signature

A rectangular box containing a redacted signature.

Farnoos Farrokhi

Electrothermal Analysis of Integrated Circuit:

A Realization by Infrared Thermography

MASc., Electrical and Computer Engineering

Ryerson University

Toronto, 2009

Abstract

The International Technology Roadmap for Silicon (ITRS) predicted that by the year 2016, a high-performance chip could dissipate as much as 300 W/cm^2 of heat. Another more noticeable thermal issue in IC's is the uneven temperature distribution. Increased power dissipation and greater temperature variation highlight the need for electrothermal analysis of electronic components. The goal of this research is to develop an experimental infrared measurement technique for the thermal and electrothermal analysis of electronic circuits. The objective of the electrothermal analysis is to represent the behavior of the temperature dependent characteristics of electronic device in near real work condition.

An infrared (IR) thermography setup to perform the temperature distribution analysis and power dissipation measurement of the device under test is proposed in this research. The system is based on a transparent oil heatsink which captures the thermal profile and run-time power dissipation from the device under test with a very fine degree of granularity.

The proposed setup is used to perform the thermal analysis and power measurement of an Intel Dual Core E2180 processor. The power dissipation of the processor is obtained by calculating and measuring the heat transfer coefficient of the oil heatsink. Moreover, the power consumption of the processor is measured by isolating the current used by the CPU at run time. A three-dimensional finite element thermal model is developed to simulate the thermal properties of the processor. The results obtained using this simulation is compared to the experimental results from IR thermography.

A methodology to perform electrothermal analysis on integrated circuits is introduced. This method is based on coupling a standard electrical simulator, which is often used in the design process, and IR thermography system through an efficient interface program. The proposed method is capable of updating the temperature dependent parameters of device in near real time.

The proposed method is applied to perform electrothermal analysis of a power MOSFET to measure the temperature distribution and the device performance. The DC characteristics of the device are investigated. The obtained results indicated that the operating point, I-V characteristics and power dissipation of the MOSFET vary significantly with temperature.

Instruction on Borrowers

Ryerson University requires the signatures of all persons using or photocopying this thesis.

Please sign below, and give address and date.

Acknowledgments

First of all, I would like to express my gratitude to my supervisor, Dr. Farah Mohammadi, for accepting me as her MASc. student in Ryerson University. Her expertise, understanding, and patience, added considerably to my graduate experience and without her excellent guidance and encouragement, it would have been so much harder to finish this research.

I would like to thank my committee members Dr. K. Raahemifar, Dr. G. Khan, and Dr. M. Jaseemuddin for their great advices and supports.

I would also like to thank my friends, Tarek Khan, Elahe Talebinejad, Tayaz Fakhri, Majid Veyseh and Aziz Rajab for all the wonderful time that we shared and their help during my research.

I would like to thank National Science and Engineering Council of Canada (NSERC) and Ryerson University for supporting and funding my research.

I would like to thank my parents, my dear aunt Monir Farrokhi and her great family whom I love with all my heart, for all their support.

Last but not least, I thank God for whatever I am and have right now.

Table of Contents

List of Figures	ix
List of Tables	xi
CHAPTER 1	1
1. Introduction.....	1
1.1 Thermal Investigation of Electronic System.....	2
1.1.1 System Level of Thermal Analysis.....	2
1.1.2 Package Level of Thermal Analysis	2
1.1.3 Component Level of Thermal Analysis.....	3
1.2 Thesis Objective.....	3
1.3 Thesis Outline	4
CHAPTER 2	5
2. Thermal Mapping	5
2.1 Liquid Crystal Thermography.....	5
2.1.1 Limitation in Liquid Crystal Thermography.....	7
2.2 Thermoreflectance Technique	8
2.2.1 Limitations in Thermoreflectance technique	10
2.3 Scanning Thermal Microscopy	10
2.3.1 Thermal sensors	11
2.3.2 Limitations in Scanning Thermal Microscopy	12
2.4 Infrared Thermography	12
2.4.1 Range within the electromagnetic spectrum.....	13
2.4.2 Radiation laws of the black body.....	14
2.4.3 Parameters affected Infrared thermography.....	15
2.4.4 Why Use Infrared thermography?	18
2.5 Summary	19
CHAPTER 3	20
3. Infrared Thermography Setup	20
3.1 Literature Review on Infrared Thermography Setup.....	21
3.2 Proposed IR thermography setup.....	26
3.2.1 Infrared Camera	26
3.2.2 Data Acquisition System.....	27
3.2.3 Heatsink	28
3.2.4 Oil Pump	32
3.2.5 Thermocouple and Digital Thermometer.....	33

3.2.6	Emissivity	33
3.2.7	Type of Analysis	34
3.3	Thermal Analysis of an Intel Dual Core E2180 Processor	35
3.3.1	Temperature Measurement	35
3.3.2	Power Measurements	36
3.4	Discussion	46
3.5	Comparison With Existing Work	47
3.6	Summary	47
CHAPTER 4	49
4.	Thermal Model of the Intel Dual Core E2180 Processor	49
4.1	Finite Element Model	49
4.2	Boundary and Subdomain Settings	52
4.3	Simulation Results	53
4.4	Summary	56
CHAPTER 5	57
5.	Electrothermal Analysis	57
5.1	Electrical Analysis	58
5.1.1	MOSFET Pspice MODEL	59
5.2	Thermal Analysis	65
5.2.1	Camera SDK	65
5.2.2	Temperature Profile by SDK	67
5.3	Methodology of IR Thermography and PSPICE Simulator Coupling	69
5.3.1	Implemented Algorithm	69
5.4	Electrothermal Analysis of a power MOSFET	71
5.4.1	Power MOSFET Electric Model	71
5.4.2	Power MOSFET IR Thermography	74
5.5	Simulation Results	76
5.5.1	DC Analysis	76
5.6	Discussion	80
5.7	Summary	81
CHAPTER 6	82
6.	Conclusions and Future Work	82
References	85
Publications	92

List of Figures

Figure 2.1: Typical reflected wavelength (color) temperature response of a TLC mixture.	6
Figure 2.2: Color-temperature distribution of an operating electronic device.....	7
Figure 2.3: Measurement setup for Thermoreflectance technique [13].....	9
Figure 2.4: Image of the micro heater under study [13].	9
Figure 2.5: Images of (a) $\Delta R/R$ and (b) ΔT for a dissipated power of 2 mW [13].	10
Figure 2.6: Scanning thermal microscopy system.	11
Figure 2.7: The infrared bands in the infrared spectrum.	13
Figure 2.8: Planck's radiation law.	14
Figure 2.9: Stefan Boltzmann's law.....	15
Figure 2.10: Spectral transmittance of air (10 m, 25 °C, 1013 mbar, 85% rel.hum.).....	16
Figure 2.11: Spectral emissivity of a few non-metals (enamel, gypsum, concrete, Chalmette)... ..	17
Figure 2.12: Spectral emittance of metals (Silver, Gold, Platinum, Rhodium, Chromium, Tantalum, Molybdenum) and other pure materials (Graphite, Selenium, Antimony).....	18
Figure 3.1: Typical IR thermography setup.	21
Figure 3.2: Spatially imaging technique and the IR-transparent cooling cell [31].....	22
Figure 3.3: Cross section diagram of the measurement setup.	23
Figure 3.4: Schematic of IR thermography measurement of component surface temperature through a polypropylene film.....	24
Figure 3.5: Measuring setup [34].....	25
Figure 3.6: Typical measurement setup.	26
Figure 3.7: Infrared camera SC4000.....	27
Figure 3.8: Thermal resistance circuit.	29
Figure 3.9: Temperature distribution of the processor with air cooling.	30
Figure 3.10: Temperature measurement with turbulent oil flow.	31
Figure 3.11: Temperature measurement with turbulent oil flow at an angle of 45°.	31
Figure 3.12: Temperature measurement with laminar oil flow.	32
Figure 3.13: Utility pump.	32
Figure 3.14: Emissivity effect on temperature measurement of the DUT.....	33
Figure 3.15: Percent error with emissivity from 0.5 to 0.7.....	34
Figure 3.16: Transient analysis of the processor, (a) 2D temperature profile at $t=57s$, (b) temperature evolution of SP01 location versus time.	36
Figure 3.17: Processor thermal characterization parameter relationships.	38
Figure 3.18: Thermal resistance for various power dissipations.	41
Figure 3.19: Average thermal resistance.	41
Figure 3.20: Temperature profile at (a) $t=32$ sec. (b) $t=41$ sec. (c) $t=60$ sec. (d) $t=73$ sec. while running the benchmark.	43
Figure 3.21: Power dissipation curve versus time.	44
Figure 3.22: Labview interface with DMM.....	45
Figure 3.23: Total power consumption waveform.....	45
Figure 3.24: Power consumption of the processor during load condition.	46
Figure 4.1: LGA 775 socket with its processor components.....	50

Figure 4.2: Finite element model (a) 2D, side view , (b) 3D view	51
Figure 4.3: Temperature profile of the FEM simulation for power dissipation of 5.5W.	54
Figure 4.4: Temperature profile of the FEM simulation for power dissipation of 18W.	55
Figure 4.5: Comparison of simulation results and [38].	56
Figure 5.1: V_{th} -T data of a $W/L=6\mu m/0.25\mu m$ n-channel MOSFET at different V_{bs} [49].	61
Figure 5.2: I-V characteristics of the drain/bulk junction at different temperatures [49].	63
Figure 5.3: $I_{ds}-V_{gs}$ curve of an n-channel MOSFET of a $W/L=6\mu m/0.25\mu m$ at different temperature after Cheng et al. [49].	64
Figure 5.4: $I_{ds}-V_{ds}$ curve of an n-channel $0.25\mu m$ MOSFET at different temperature after Cheng et al. [49].	65
Figure 5.5: Camera SDK diagrams [52].	67
Figure 5.6: Flowchart of the electrothermal analysis.	70
Figure 5.7: Schematic of the MOSFET.	71
Figure 5.8: MOSFET DC characteristics.	72
Figure 5.9: MOSFET thermal profile with oil heatsink, (a) 2D temperature profile, (b) temperature profile versus time	74
Figure 5.10: MOSFET thermal profile without oil heatsink, (a) 2D temperature profile, (b) temperature profile versus time.	75
Figure 5.11: MOSFET DC characteristic with updating temperature with cooling system (a) ID versus V_{DD} , (b) ID versus temperature.	77
Figure 5.12: MOSFET power dissipation with updating temperature with cooling system, (a) Power versus V_{DD} , (b) Power versus temperature.	78
Figure 5.13: MOSFET DC characteristic with updating temperature without cooling system.	79
Figure 5.14: MOSFET power dissipation with updating temperature without cooling system. ...	79
Figure 5.15: $R_{DS(on)}$ of MOSFET during DC analysis without oil cooling system versus temperature.	81

List of Tables

Table 3.1: Specification of the cooling system.....	37
Table 4.1: Material properties and dimentions of layers of the thermal model of the LGA processor and its sockets.....	52

Chapter 1

1. Introduction

Technology scaling and increasing circuit density (Moore's law) will continue in spite of tremendous technology development barriers, design challenges, and prohibitive costs. Miniaturization of electronic devices and circuits has lead to the emergence of self-heating as a critical bottleneck to the performance and reliability of emerging electronic circuits and systems. Consequently, thermal management has become one of the most challenging factors in modern electronic design.

The continuous and aggressive scaling of CMOS IC technology has resulted in higher performance at the expense of higher power consumption, higher operating temperatures and reduced reliability. Furthermore, local hot spots, which have much higher temperatures compared to the average die temperature, are becoming more prevalent in VLSI circuits. If heat is not removed at a rate equal to or greater than its rate of generation, junction temperatures will rise, reducing mean time to failure (MTTF) for the devices [1]. Device reliability has a direct impact on the overall system reliability. Removing heat from these devices is thus a major task facing design engineers of modern electronic systems concerned with improving reliability [2] and electrothermal analysis has become an important part of modern electronic design enabling designer to calculate the critical thermal variables as key factors in electrical analysis and accurate performance [3].

The key to successful thermal management is the ability to obtain comprehensive and accurate prediction of temperature gradients influencing the quality of electronic products under near real-time operating conditions. However, the commonly used method of gathering these temperature

gradients using thermocouples is limited by the large number of points to be monitored and the small size of the components being measured. Connecting tens to hundreds of thermocouples is very time consuming. Also, thermocouples can act as heatsinks and conduct away heat, affecting the accuracy of measurements since the action of the heatsink may lower device temperatures.

Infrared (IR) thermal imaging system is a method which addresses the above-mentioned issues by providing comprehensive two-dimensional temperatures gradients of components under test. This is accomplished without the need to make contact with the components.

1.1 Thermal Investigation of Electronic System

There are three levels of thermal analysis (experimental and/or numerical) and depending on the level of the design an electronic designer is engaged, one of these analyzing levels must be chosen that gives out only the sufficient and relevant information about the thermal behaviour of the subject of the thermal analysis. These levels are as follows:

1.1.1 System Level of Thermal Analysis

Accurate experimental and/or numerical thermal analysis of a complex electronic system including several packages, discrete elements, printed circuit boards, connectors and mechanical parts, heatsinks and cooling mechanism, and enclosure is almost impossible with existing experimental, analytical and numerical techniques, because of its complexity and the large number of thermal characteristics affecting the thermal behaviour of the system and the output of the analysis includes large amount of unnecessary information. The alternative solution is to perform experimental and/or numerical analysis of packages, boards, devices and other parts of the system separately and use them as the building blocks of the thermal analysis of the system. This system level model then generates the thermal variables of the desired locations within the system.

1.1.2 Package Level of Thermal Analysis

This level of thermal analysis is useful when the electronic designer needs to calculate the temperature profile and inward/outward heat fluxes of an electronic package working as a part of an electronic system. A package can be analyzed thermally using IR experimental analysis or

numerical simulation software. One of the subjects of this thesis is thermal analysis (experimental and numerical) in package level which will be explained thoroughly in Chapters 3 and 4. Detailed IR experimental analysis of package provides a relatively accurate temperature profile for every location on the surface of package.

1.1.3 Component Level of Thermal Analysis

At the component level a single component or some specific components of the electronic circuit are the subjects of thermal analysis. It's desirable for the designer to study the effect of thermal behaviour of components on their own electrical behaviours and the mutual effects of the thermal behaviours of components on the electrical behaviours and operating points of their adjacent components. This level of analysis is usually used in electrothermal analysis of the electronic circuit [5]. When there are some components which play key roles in the circuit and it's critical for the designer to predict their electrical and thermal operating points in order to design a stable, predictable, and reliable circuit, electrothermal analysis of the circuit is necessary.

Unlike ordinary electrical analysis by which the electrical operating point of the circuit is calculated for a fixed and predetermined temperature (usually room temperature), electrothermal analysis performs both electrical and thermal analyses concurrently. It is well known that electrical current flowing through the materials causes heat dissipation and temperature elevation. This phenomenon is called Joule heating and in most cases changes the electrical operating point of the component and the circuit in which it is operating. Electrical analysis with fixed temperature, thus, is not sufficient for an accurate analysis. Electrothermal analysis should be performed so the effects of temperature variation and electrical operating point variation are taken into the consideration. This is the subject of Chapter 5 of this thesis.

1.2 Thesis Objective

The goal of this research is to develop an infrared thermography infrastructure for the electrothermal analysis of electronic circuits. This research project aims to create a method to enable accurate assessment of thermal parameters affecting performance in electronic components. The thesis focuses on electrothermal analysis at package and component levels.

An IR thermography measurement setup, based on an infrared transparent oil heatsink, is developed to capture run-time power dissipation and thermal characteristics from modern processors. In addition this work aims to couple the thermal profile of the electronic device obtained by thermography with electrical model of the device to perform the electrothermal analysis and acquire the temperature dependent parameters.

1.3 Thesis Outline

In this research important subjects required for thermal mapping and electrothermal analysis of electronic devices are covered.

Advantages and disadvantages of different thermal mapping techniques are discussed in Chapter 2. In Chapter 3 different infrared thermography setups are discussed and the proposed infrared setup measurement to measure the temperature profile and power dissipation of the device under test (DUT) is introduced. The proposed measurement setup is used to capture the temperature distribution and power dissipation of a Dual Core processor. The numerical analysis of the processor is performed using finite element software (COMSOL) in Chapter 4. Chapter 5 concentrates on the proposed electrothermal analysis method by coupling IR thermography technique with an electrical simulator and the experimental results of designed electrothermal analyzer on a power MOSFET is presented. Finally, the conclusions and suggested future works are summarized in Chapter 6.

Chapter 2

THERMAL MAPPING

This chapter is an introduction to different types of thermal mapping and recent advances which have taken place in this area.

2. Thermal Mapping

Thermal mapping can be used to give visual information about temperature gradient and heat fluxes on the surface of a chip to observe, for example, the preferred location of a typical failure and to understand the thermal dynamics that lead to it. Many methods of thermal sensing can be exploited to monitor the superficial temperature gradient of an IC and they can be categorized with respect to their invasiveness, spatial and thermal resolution, bandwidth and temperature range. Hereunder some of the most important and widespread techniques are presented along with their peculiar features [8].

2.1 Liquid Crystal Thermography

Thermochromic liquid crystals (TLC) are temperature indicators that modify incident white light and display color whose wavelength is proportional to temperature. They can be painted on a surface or suspended in the fluid and used to make visible the distribution of temperature.

Normally clear, or slightly milky in appearance, liquid crystals change in appearance over a narrow range of temperature called the “color-play interval” (the temperature interval between

first red and last blue reflection), centered around the nominal “event temperature.” These color changes are repeatable and reversible as long as TLCs are not physically or chemically damaged. The response time of TLCs equals about 10 ms.

The displayed color is red at the low temperature margin of the color-play interval and blue at the high end (Fig. 2.1). Within the color-play interval, the colors change smoothly from red to blue as a function of temperature. Pure liquid crystal materials are thick, viscous liquids, greasy and difficult to deal with under most heat transfer laboratory conditions [9].

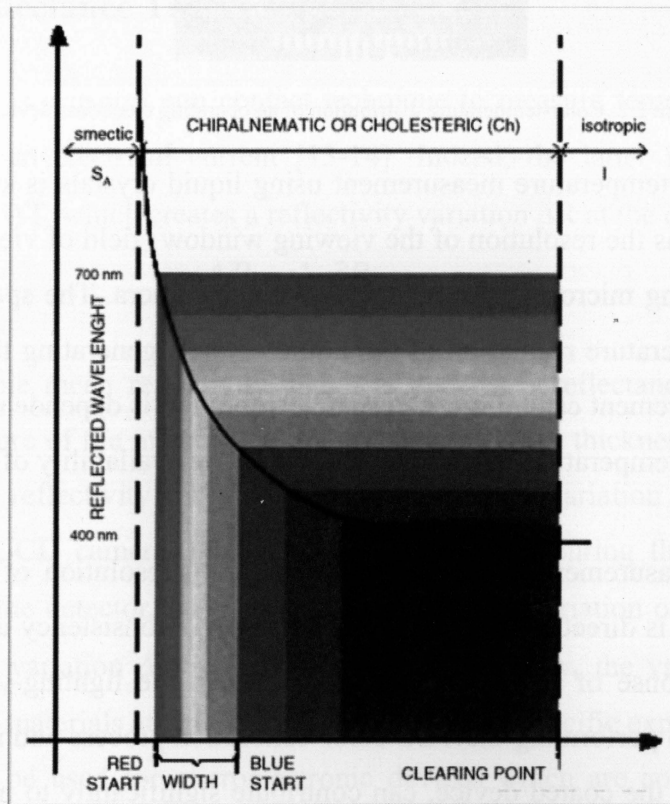


Figure 2.1: Typical reflected wavelength (color) temperature response of a TLC mixture.

Spot values or temperature distribution is determined by comparing the image from the object with the calibrated data. To facilitate data analysis and enhance accuracy, both the calibration and test images are stored electronically. These images are first digitized and a software program compares the two based on the pre-specified spatial resolution. The result of this comparison is a detailed temperature distribution map of the electronic part [10].

The color-temperature distribution of an operating electronic device measured by this method is shown in Fig. 2.2.

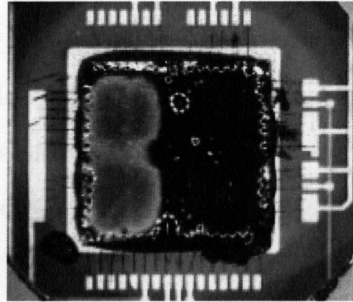


Figure 2.2: Color-temperature distribution of an operating electronic device.

The accuracy of the temperature measurement using liquid crystals is strongly dependent on the calibration as well as the resolution of the viewing window (field of view). The field of view can be obtained by using microscopic optics with a video camera. The spatial resolution of the field of view and temperature resolution of the liquid crystals generating the image, defines the boundary of the measurement capability. The spatial resolution is dependent on the liquid crystal and the hardware. The temperature resolution is based on the availability of a given liquid crystal mixture [11].

The temperature measurement accuracy and temperature resolution of measurements made with LC thermography is directly related to the accuracy and consistency used in calibrating the color-temperature response of the TLC. Inconsistencies in the lighting-viewing arrangements that are presented when performing the TLC color-calibration process and interpreting the actual TLC color response of the coated device, can contribute significantly to measurement errors in LC thermography. The optical setup includes the lighting-viewing arrangement and wavelength spectrum of the white light source.

2.1.1 Limitation in Liquid Crystal Thermography

This method can be considered a very simple, fast and cheap technique, but loses in terms of dynamics, transients must be slower than 0.1 sec, and is not contactless. Obtaining accurate and high resolution temperature measurements with LC thermography requires the proper

combination of the color-temperature response characteristics of a TLC material and the consistent use of image acquisition and interpretation.

In addition, the highest spatial resolution achievable with LC thermography is limited by the type of TLC formulation and resolving capability of the optical system (camera and lenses). Unencapsulated TLC formulations [10] coupled with high performance microscope optics can provide sub-micron spatial resolution over reasonably sized fields of view.

2.2 Thermoreflectance Technique

Thermoreflectance is a useful non contact technique to measure temperature variations of a device submitted to an electrical current [13-14]. Indeed, the latter is then submitted to a temperature variation ΔT , which creates a reflectivity variation ΔR at the device surface [15]:

$$\frac{\Delta R}{R} = \frac{1}{R} \frac{\partial R}{\partial T} \Delta T = k \Delta T \quad (2.1)$$

where R is the sample mean reflectivity and k is the thermoreflectance coefficient which is dependent on the nature of the material, on the passivation layer thickness [14] and on the light wavelength [16]. The reflectivity variation implies an intensity variation of the light reflected to the photo detector (CCD camera, photodiode). Thus, by measuring the relative variation of photocurrent $\Delta I/I$ of the detector, we can deduce the relative variation of reflectivity $\Delta R/R$ and then the temperature variation ΔT if k is known. Unfortunately, the value of k is often only known for a few bulk materials at a precise wavelength under specific experimental conditions.

This value cannot be used for microelectronic devices which are covered with passivation layers whose thickness has a great influence on k . As k depends on the microelectronic structure and on experimental conditions (wavelength illumination), every studied sample and every experimental setup need a new calibration. Once the value of k is determined, one can obtain quantitative temperature variations.

The setup to measure thermomechanical behavior of a biased microelectronic heater is presented in Fig. 2.3. One arm of the interferometer is used as a reference arm whereas the second one (object arm) is ended by the device under test. The luminous source is a red LED

with a 6° dispersion angle. An interferential filter (IF) reduces the spectrum of emission of the LED and improves the spectral purity of the light source, which enables one to increase the coherence length. The lens (L_1) enables one to adapt the size of the luminous beam to the size of the object under study. As we use a polarizing beam splitter (PBS) and as the light emitted by the LED is unpolarized, a sheet polarizer (P_1) is used to polarize it and to balance the light intensity in both arms of the interferometer.

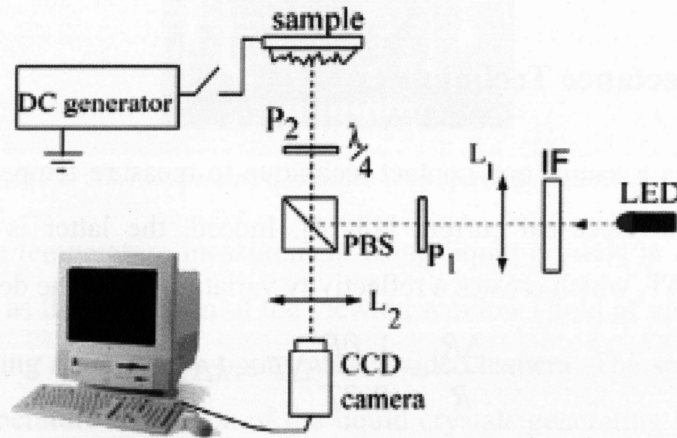


Figure 2.3: Measurement setup for Thermoreflectance technique [13].

An optical image of the sample is presented in Fig. 2.4.

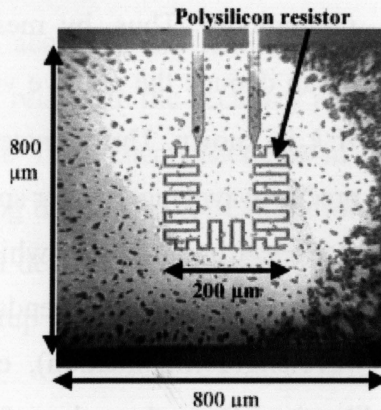


Figure 2.4: Image of the micro heater under study [13].

Using the thermoreflectance imaging technique, a relative reflectivity variation image of the central part of the device has been obtained (Fig. 2.5a) and once both polysilicon and dielectric

thermoreflectance coefficients are known, a quantitative temperature variation image can be obtained (Fig. 2.5b).

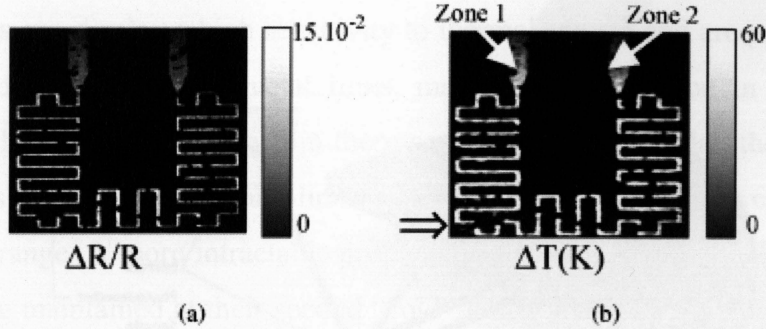


Figure 2.5: Images of (a) $\Delta R/R$ and (b) ΔT for a dissipated power of 2 mW [13].

2.2.1 Limitations in Thermoreflectance technique

The challenge of the thermoreflectance method is to resolve the small change in the reflection coefficient. Typically for metals, the reflection coefficient only changes by about 1/105 for each degree Celsius change in surface temperature. For high resolution thermal measurements it is necessary to use a high gain photodiode and lock-in amplifier, while thermally cycling the active device at a known frequency [17].

2.3 Scanning Thermal Microscopy

Another method for directly measuring the microscopic thermal properties of a surface is to use Scanning Thermal Microscopy (SThM) [18], which is capable of simultaneously acquiring thermal and topographic images (see Fig. 2.6).

The requirements of SThM in the context of thermometry are additionally that the sensor be susceptible to meaningful calibration and should not only have high spatial resolution, but the sensitivity to temperature should rapidly fall to as close to zero as possible at distances significantly in excess of that resolution [19].

These requirements, coupled with the ability to measure electrically live specimens are particularly relevant when imaging semiconductor devices, which often have lifetimes

determined by thermal management and so are particularly relevant for study using SThM. No existing SThM system possesses all of these desirable characteristics [20].

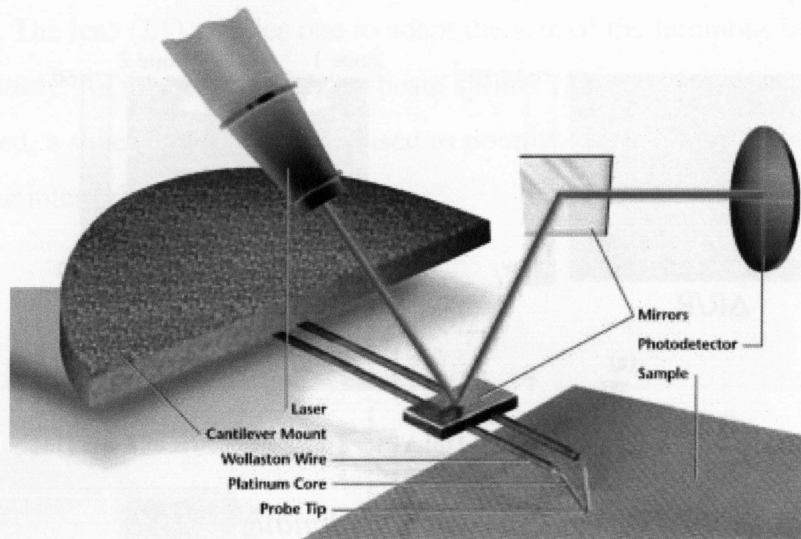


Figure 2.6: Scanning thermal microscopy system.

2.3.1 Thermal sensors

Various sensors have been employed in SThM, these include Schottky diodes [21], resistors [22] and thermocouples [23]. Each has strengths and weaknesses, with the major factors as explained next.

- **Schottky diodes** offer high sensitivity and straightforward fabrication on a silicon probe. Less ideally, they are light sensitive and the semiconducting probe has relatively high thermal conductivity. Calibration of a Schottky diode thermometer is necessary due to the need to compensate for non-ideal diode characteristics.
- **Resistors** are well-established thermal sensors, are stable and display a near linear response to temperature change. This makes them well suited to calibration. They can be fabricated from deposited metal films or doped semiconductors and so are amenable to integration into most conventional probe fabrication schemes. Less desirable for thermometry is the fact that their measurement results in Joule heating, so that some tradeoff between sensitivity and self-heating

must be made in use. Along with Schottky diodes, however, this self heating may be usefully applied to the measurement of thermal conductivity.

- **Thermocouples** can display a high sensitivity to thermal change and are passive sensors. They can be fabricated from deposited metal films, making their inclusion in a probe fabrication procedure possible. Regrettably, thin film thermocouples seldom display the sensitivity of their bulk counterparts and they have a non-linear thermal response, requiring calibration over their whole operating range. A more intractable problem is that their operation relies upon a constant temperature being maintained at their second “cold” junction. This can be impossible to achieve when scanning a small SThM probe in very close proximity to a much larger, hot substrate.

2.3.2 Limitations in Scanning Thermal Microscopy

Scanning thermal microscopy (SThM) is an effective tool for temperature and energy dissipation measurements. However, because the contacted thermocouple or heated probe tip scans the specimen surface, the resolution is not high, and the dissipation of energy is caused. To solve this problem, researchers use SThM by integrating a thermal sensor into the tip of an Atomic Force Microscopy (AFM). Atomic Force Microscopy is the technique that gives the best spatial and thermal resolution but is also the most expensive. The atomic repulsive forces between a micromachined probe and the surface of the DUT are measured by an optical system. The signal retrieved can be related to the surface temperature. With such a system spatial resolutions in the order of tenths of nanometer and temperature sensitivities around 5°C can be achieved. Nonetheless bandwidth is limited compared to laser techniques [24].

2.4 Infrared Thermography

All objects radiate infrared energy proportional to their temperature. Infrared imaging systems convert infrared heat emissions into a picture that shows the relative temperature differences in a range of gray tones or a series of colors. Most conditions in which an anomaly is characterized by an increase or decrease in surface temperature or retained residual heat are detectable with infrared thermography [25].

2.4.1 Range within the electromagnetic spectrum

Infrared radiation is that part of the electromagnetic spectrum that is immediately adjacent to the red light of approx. 760 nm on the long-wave side of the visible spectrum and extends to a wavelength of approximately 1 mm (see Fig. 2.7). In this respect, the wavelength range of up to approx. 20 μm is of importance to technical temperature measuring. In the second half of the 19th century, it became known that heat radiation and other electromagnetic waves, such as visible light or radio waves were similar in nature. This was followed by the discovery of the laws of radiation by Kirchhoff, Stefan, Boltzmann, Wien and Planck. By the mid-20th century, intensive and successful work on the military use of infrared technology facilitated the building of first infrared viewers.

Later the first thermographic devices for non military application became available in the 60s. Parallel to this, however, in considerably larger diversification of available devices, pyrometry developed to become a wide-spread approach in industrial temperature measuring.

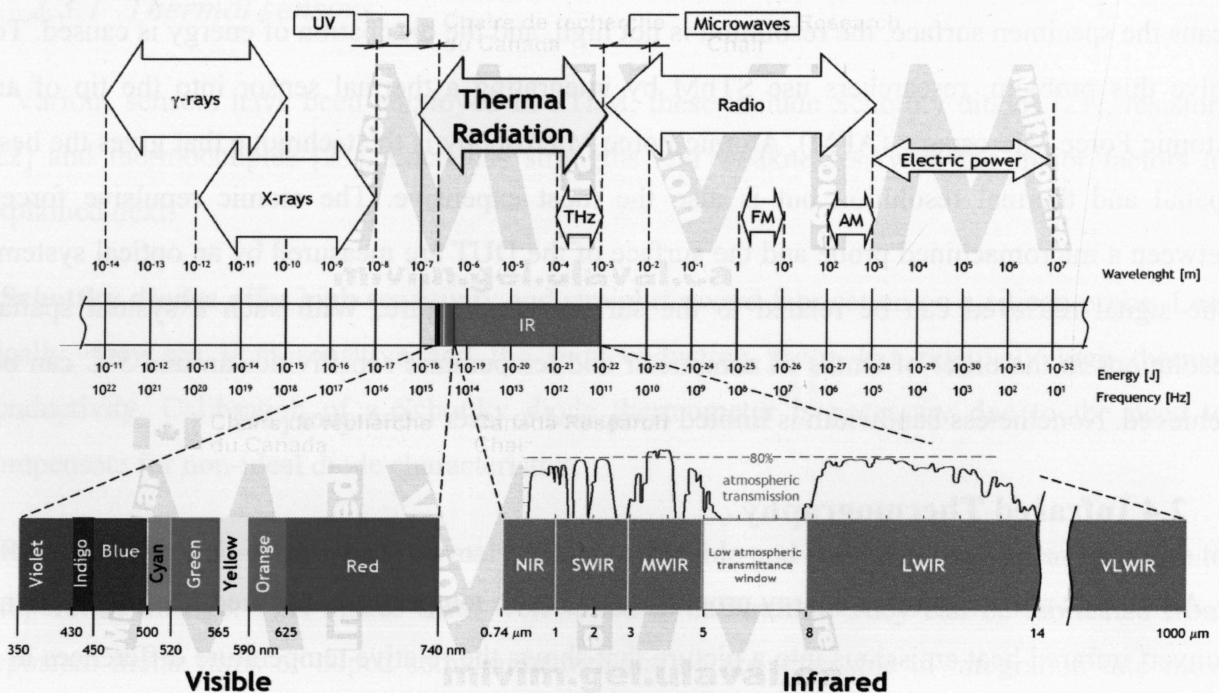


Figure 2.7: The infrared bands in the infrared spectrum.

2.4.2 Radiation laws of the black body

The bodies occurring in real life show very diverse radiation properties. Therefore, it has proved worthwhile to initially consider the simplified laws of a model body of ideal radiation properties to be then applied to actually occurring objects. This model body is known in radiation physics as the “black body.” It distinguishes itself by the fact that, of all bodies of equal temperature, it shows the largest possible emitted radiation. The spectral spread of radiation emitted by a black body is described by Planck’s radiation law:

$$M_{\lambda} = \frac{C_1}{\lambda^5 \times \left[\exp\left(\frac{C_2}{\lambda T}\right) - 1 \right]} \quad (2.2)$$

where $C_1 = 3.74 \times 10^{-16} \text{ Wm}^2$ and $C_2 = 1.44 \times 10^{-2} \text{ Km}$.

Figure 2.8 shows that the spectral composition varies with the object temperature. Bodies of a temperature of beyond 500 °C, for example, also emit radiation in the visible range. Furthermore, it must be noted that, at each wavelength, radiation intensity increases with rising temperature.

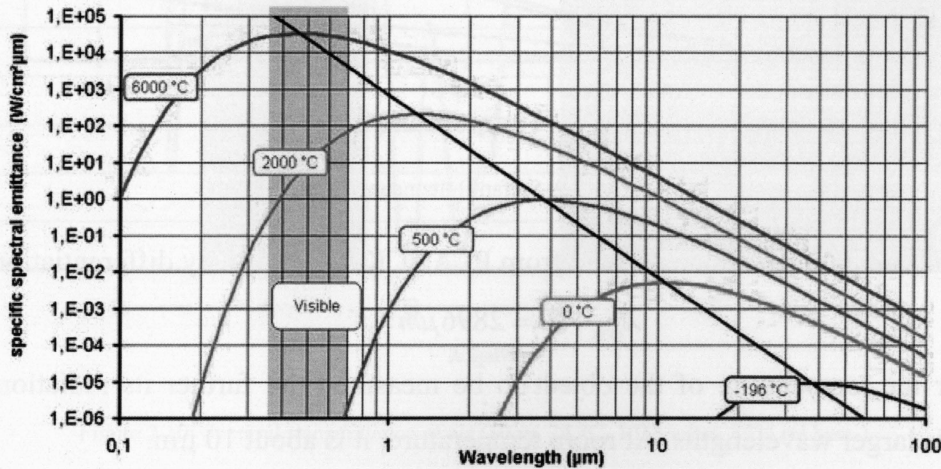


Figure 2.8: Planck’s radiation law.

Planck’s radiation law represents the principal correlation regarding non-contact temperature measuring. Due to its abstract nature, however, it is not directly applicable in this form to many practical calculations. But a variety of further correlations can be derived from it, two of which shall briefly be mentioned in the following. By means of integrating the spectral radiation

intensity across all wavelengths, the value of the entire radiation emitted by the body is obtained. This correlation is called the STEFAN BOLTZMANN's law (Fig. 2.9).

$$M = \sigma T^4 \quad (2.3)$$

Due to its simple mathematical correlation, it is well suited for rough estimates, particularly when calculating the heat balance of objects as well as interrelations of total radiation pyrometers. However, the spectral measuring range of most measuring devices is usually strongly limited and, therefore, this equation is inapplicable to this research.

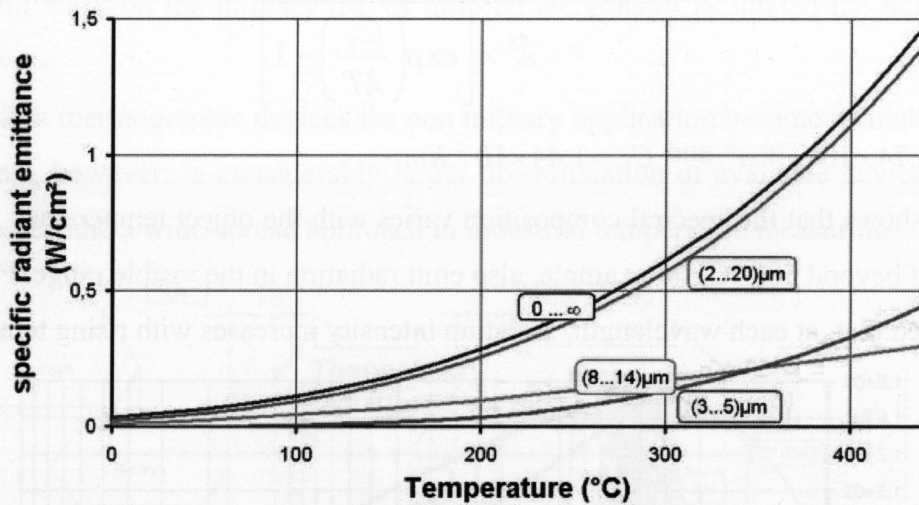


Figure 2.9: Stefan Boltzmann's law.

WIEN's displacement law can be derived from PLANCK's equation by differentiation.

$$\lambda_{\max} \times T = 2896 \mu\text{m} \times K \quad (2.4)$$

The lower the temperature of the object to be measured the further its radiation maximum shifts towards larger wavelengths. At room temperature, it is about 10 μm.

2.4.3 Parameters affected Infrared thermography

a) Measuring distance

Since infrared thermography is a non-contact procedure, infrared radiation needs to travel over a certain distance between the object to be measured and the measuring device through a

medium whose infra optical properties may affect the measured result. In most cases, this medium is likely to be air, but also other materials, such as infrared-transmittant "windows" occur in real life. In the case of air, its components, such as water vapour and carbon dioxide, affect its infrared transmittance.

The level of transmittance of air (see Fig. 2.10) is strongly dependent on wavelength. Ranges of high attenuation alternate with ranges of high transmittance (shaded), the so-called "atmospheric windows." While transmittance in the range of (8...14) μm , i.e., the long-wave atmospheric window, maintains to be equally high over longer distances, measurable attenuation caused by the atmosphere already occurs in the range of (3...5) μm , i.e., the short-wave atmospheric window, at measuring distances of some ten meters.

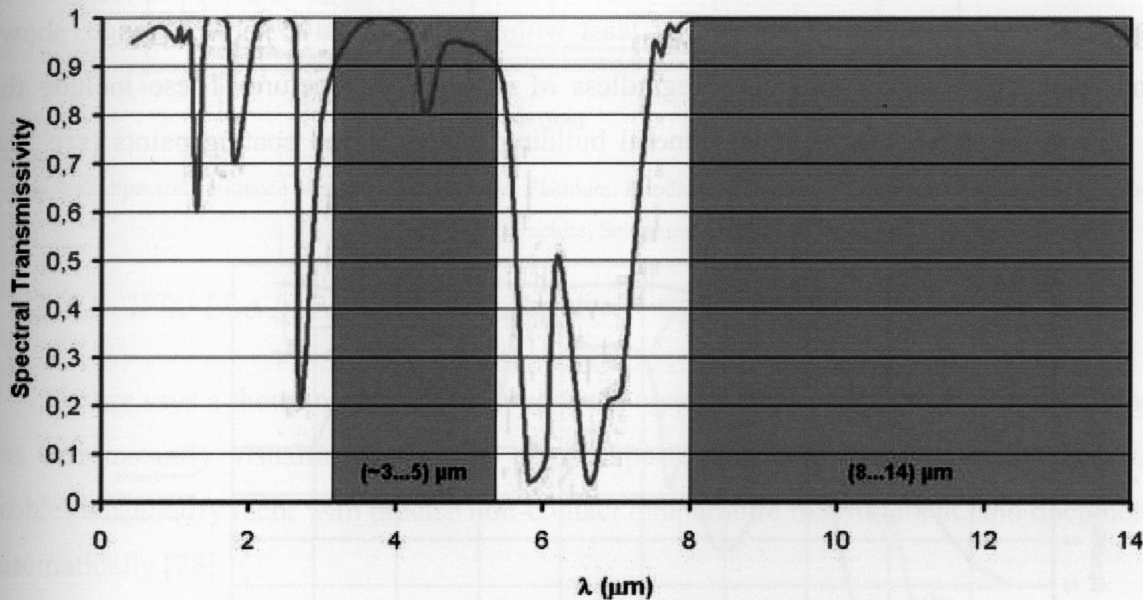


Figure 2.10: Spectral transmittance of air (10 m, 25 °C, 1013 mbar, 85% rel.hum.).

b) Measured Object

The black body as a radiometric model is indispensable when considering principal correlations. Since real objects that are to be measured deviate more or less strongly from that model, it may become necessary to take this influence into account in measurements. Especially suited for this purpose is the parameter of emittance which is the measure for a body's capability

of emitting infrared radiation. Having a value of 1, the black body has the highest possible emittance, which is additionally dependent on wavelength. Contrary to this, the emittance of real objects to be measured may show more or less strong dependence on wavelength. The following parameters may also be of some influence:

- Material composition
- Oxide film on the surface
- Surface roughness
- Angle to the surface normal
- Temperature
- Polarisation degree

A multitude of non-metallic materials, at least within the long-wave spectral range, shows high and relatively constant emittance regardless of its surface structure. These include the human skin in the same way as most mineral building materials and coating paints (see Fig. 2.11).

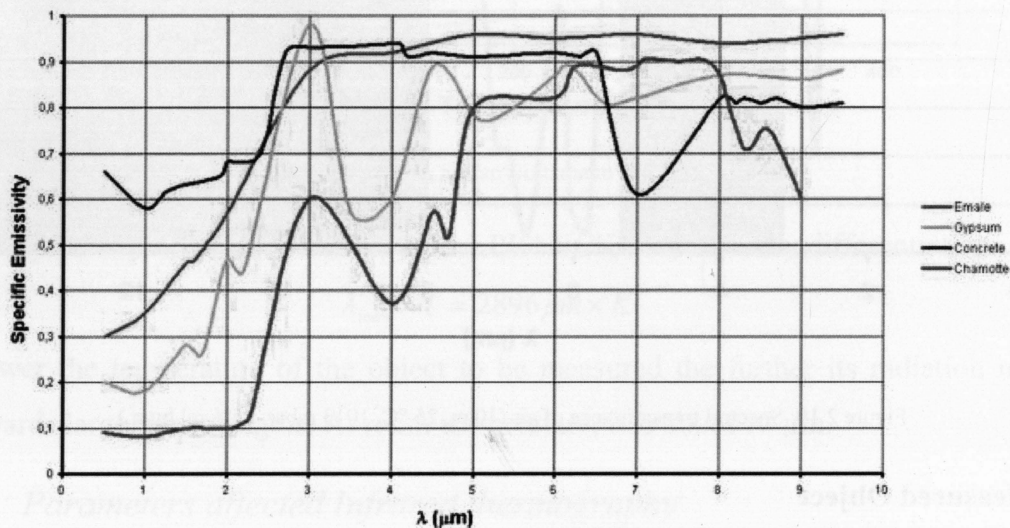


Figure 2.11: Spectral emissivity of a few non-metals (enamel, gypsum, concrete, Chamotte).

In contrast, metals generally have low emissivity that greatly depends on the surface properties and drops as wavelengths increase (see Fig. 2.12).

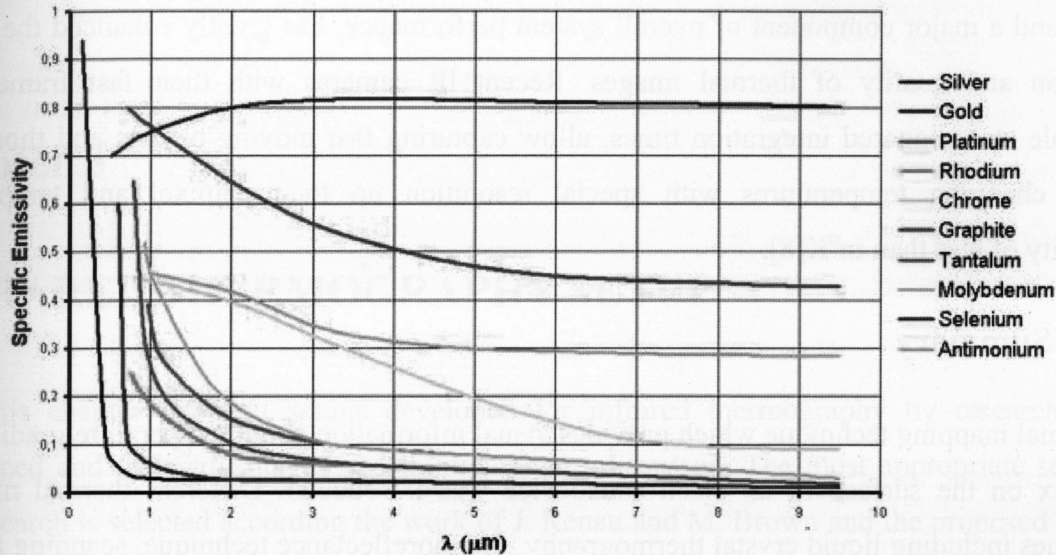


Figure 2.12: Spectral emittance of metals (Silver, Gold, Platinum, Rhodium, Chromium, Tantalum, Molybdenum) and other pure materials (Graphite, Selenium, Antimony).

2.4.4 Why Use Infrared thermography?

A picture says a thousand words; infrared thermography is the only diagnostic technology that lets one instantly visualize and verify thermal performance. Infrared cameras show thermal problems, quantify them with precise non-contact temperature measurement, and document them automatically [28].

An infrared camera is a non-contact device that detects infrared energy (heat) and converts it into an electronic signal, which is then processed to produce a thermal image on a video monitor and perform temperature calculations. Heat sensed by an infrared camera can be accurately quantified, or measured, allowing one to not only monitor thermal performance, but also identify and evaluate the relative severity of heat-related problems. Recent innovations, particularly detector technology, the incorporation of built-in visual imaging, automatic functionality, and

infrared software development, deliver more cost-effective thermal analysis solutions than ever before [27].

The innovative focal plane array (FPA) sensor, which is the heart of any infrared camera system and a major component of overall system performance, has greatly enhanced the spatial resolution and quality of thermal images. Recent IR cameras with their fast frame rates, adjustable and triggered integration times, allow capturing fast moving objects and those with rapidly changing temperatures with special resolution up to megapixel and temperature sensitivity of less than $m^{\circ}K$ [8].

2.5 Summary

Thermal mapping technique which provides visual information about temperature gradient and heat flux on the surface of an electronic device was introduced. Different thermal mapping techniques including liquid crystal thermography, thermoreflectance technique, scanning thermal microscopy and infrared thermography were discussed and their setup measurement, advantages and limitation were reviewed. Infrared thermography which is a none contact thermal mapping technique was selected for our application in this project.

Chapter 3

INFRARED THERMOGRAPHY SETUP

In this chapter different setups developed for infrared thermography by researchers are introduced and their advantages and limitations are discussed. The most appropriate setup for this research is selected according the work of J. Renau and M. Brown and the proposed setup is used to obtain the test results of an Intel Dual Core E2180 processor in terms of temperature gradient and power dissipation.

3. Infrared Thermography Setup

The thermally sensitive parameters vary according to the type of semiconductors used and, thus, would require a unique measurement setup and calibration procedure for systems using different type for electronic devices [29].

Several points should be considered in experimental setup for infrared thermography. Atmospheric temperature, reflected temperature, emissivity, distance of measurement, relative humidity and the reference temperature. Different setups have been explained in the literature which will be discussed in details, but nobody has clearly explained all these conditions prevalent during the performance of their experiments.

3.1 Literature Review on Infrared Thermography Setup

The setup for infrared thermography that permits the removal of heat from the backside of an integrated circuit semiconductor substrate while performing optical based testing through or at the backside surface of the semiconductor substrate was described by [30].

The electronic device is to be kept upside down as emission from the back side of an integrated circuit may be measured to determine a variety of defects such as impact ionization, shorts, hot carrier effects, forward and reverse bias P-N junctions, transistors in saturation and gate oxide breakdown. Figure 3.1 shows a typical setup for infrared thermography. Heatsink is thermally coupled to the outer edges of the heat slug's top surface. Heat slug has to be infrared transparent and so it is usually made of diamond as it is excellent conductor of heat and infrared transparent as well. However, depending upon the application, the material used for the heat slug can be changed, i.e. sapphire, germanium and gallium arsenide, etc. Heatsink may include metal plate (e.g. aluminum, copper). The only constraint is that the binding used for heatsink should have a large thermal mass and a large heat transfer area. Thermal grease or oil can be placed between heatsink and heat slug as a heat transfer medium to reduce thermal resistance at these interfaces. Here the electronic device is mounted on Pin Grid Array (PGA) with the ball bonds.

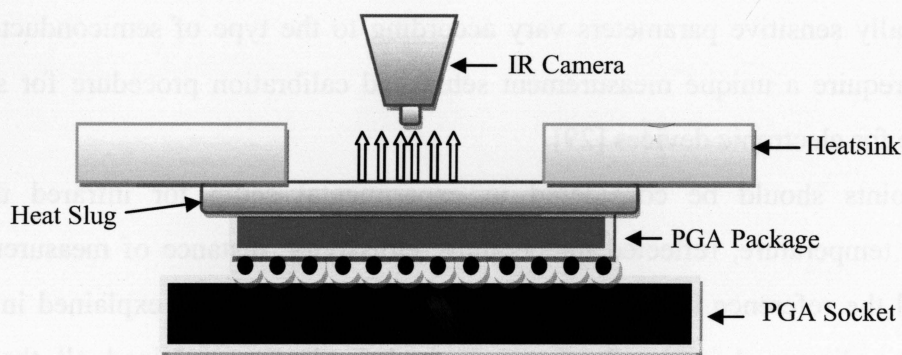


Figure 3.1: Typical IR thermography setup.

This work relied on a diamond heat spreader, but the actual cooling rates of this heatsink are typically not sufficient for high power, state of the art microprocessors running full workloads. In

addition, this diamond heat spreader involves an interface between the Si chip and the heat spreader, which is naturally difficult to control.

A more recent infrared thermography setup was proposed by [31] in 2006. As illustrated in Fig. 3.2, an IR transparent liquid flows through a micro-duct of a specifically designed cooling cell *directly* over the microprocessor die. The duct height as well as the flow speed can be adjusted, which allows for different cooling rates can be readily tuned between $0.2 \text{ W/cm}^2\text{K}$ all the way up to $4.0 \text{ W/cm}^2\text{K}$ depending on the choice of the fluid and flow conditions.

While the variable cooling rates provide the opportunity to investigate power and temperature distributions under various cooling and operating conditions and to trigger thermal and power management schemes of the chip to study their effectiveness, high cooling rates are especially important for several other reasons.

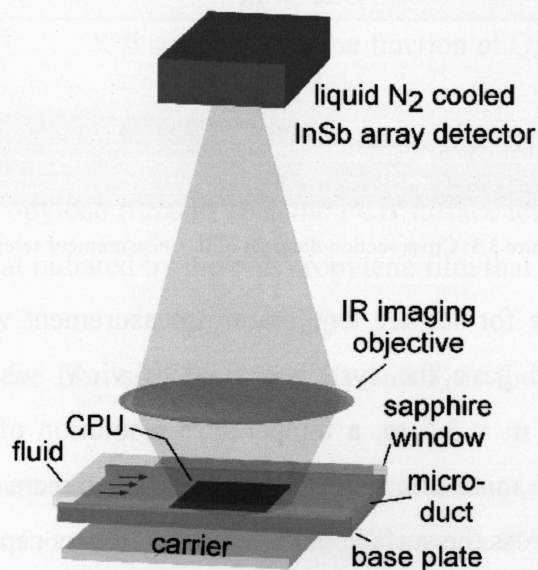


Figure 3.2: Spatially imaging technique and the IR-transparent cooling cell [31].

Hamann proposed the new method that provided real time temperature mapping of fully operating electronic devices [32]. The method utilizes infrared (IR) temperature imaging, while an IR-transparent coolant flows through a specially designed cell directly over the electronic device.

The cross section diagram of the measurement setup is shown in Fig. 3.3. In some cases it maybe preferred to use thermal reflectance to monitor the temperature of the electronic device, such as photon detector which detects the amount of reflected photons from electronic device which changes optical reflectivity with temperature. To remove the heat from device under test a fluid is passed through a duct. The wall of the duct and fluid should be at least semi-transparent to infrared radiation. This setup creates a thermal profile of the top surface of the chip.

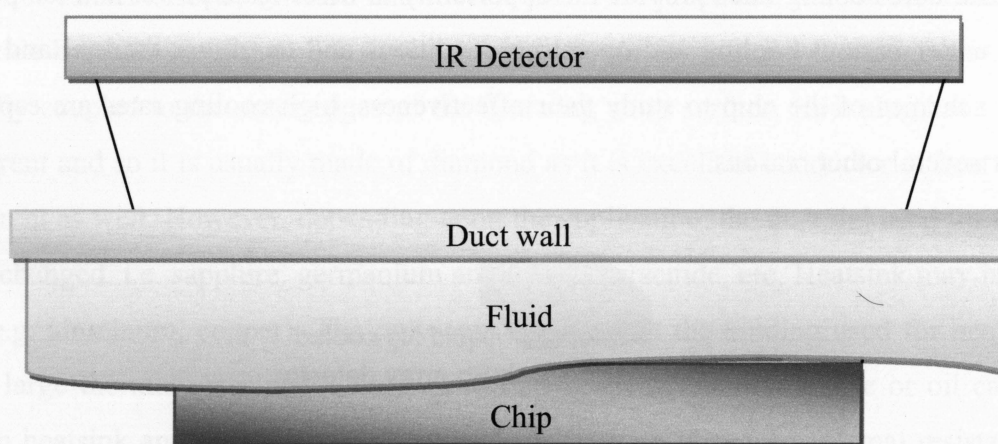


Figure 3.3: Cross section diagram of the measurement setup.

Another optical technique for surface temperature measurement was proposed by [33]. The scanner lens that was used gave the system a field of view, which could be varied from $120 \text{ mm} \times 120 \text{ mm}$ to $3.5 \text{ m} \times 3.5 \text{ m}$, a temperature resolution of $0.7 \text{ }^{\circ}\text{C}$ and a geometrical resolution of 0.86 mm at the minimum field of view. The IR camera field of view was arranged such that the temperature across the surface of the entire PCB was captured.

The material in the system wall between the IR camera and the PCB had to be transmissive for the surface temperature to be measured. A polypropylene film, calibrated against a thermocouple, met this requirement. Figure 3.4 shows a schematic of the experimental setup. From this schematic, radiative heat can be seen to reach the IR camera from three separate sources:

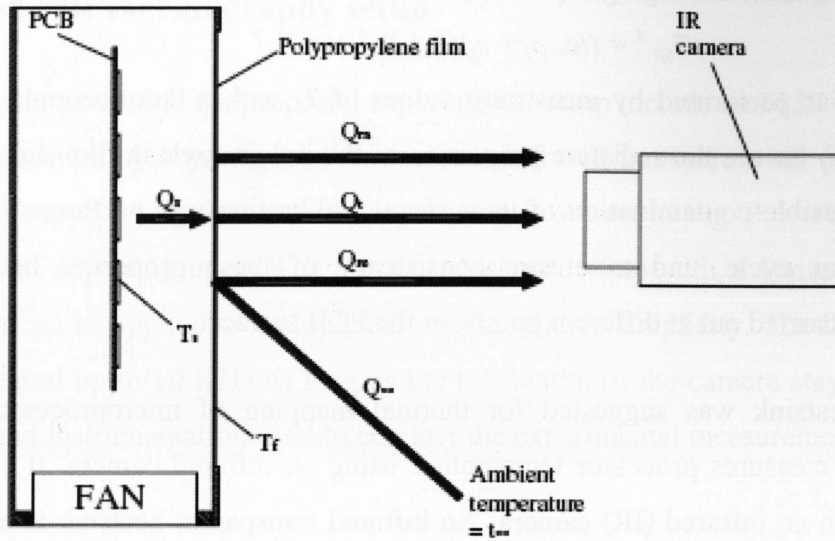


Figure 3.4: Schematic of IR thermography measurement of component surface temperature through a polypropylene film.

- (1) Q_s is the heat radiated by the PCB surface. Q_t is the fraction of Q_s that reaches the camera.

$$Q_t = \tau_f Q_s = \tau_f \sigma \epsilon_s T_s^4 \quad (3.1)$$

where σ is the Stefan-Boltzmann constant, ϵ_s is the PCB surface emissivity, τ_f is the transmissivity of the polypropylene film and T_s is the PCB surface temperature.

- (2) Q_{ra} is the quantity of heat radiated by the polypropylene film that reaches the camera:

$$Q_{ra} = \sigma \epsilon_f T_f^4 \quad (3.2)$$

where ϵ_f is the polypropylene film surface emissivity and T_f is the polypropylene film surface temperature.

- (3) Q_{∞} is the amount of heat radiated by background surfaces. Q_{re} is the quantity of that heat which is reflected off the surface of the polypropylene film to the IR camera:

$$Q_{re} = \rho_f Q = \rho_f \sigma \epsilon_{\infty} T_{\infty}^4 \quad (3.3)$$

where ϵ_{∞} is the background surface emissivity, ρ_f is the polypropylene surface reflectivity and T_{∞} is the background surface temperature.

The total heat radiated to the IR camera is therefore:

$$Q_T = \sigma \epsilon_s \tau_f T_s^4 + \sigma \epsilon_f T_f^4 + \sigma \epsilon_{\infty} \rho_f T_{\infty}^4 = \sigma \epsilon_s T_{ap}^4 \quad (3.4)$$

where T_{ap} is the PCB surface temperature which is apparent to the IR camera as a result of the radiation Q_T which reaches it. This is the uncalibrated temperature which the IR camera reads.

Assuming $T_f \approx T_\infty$ and rearranging Eq. (3.4) gives

$$T_{ap}^4 = ((\varepsilon_\infty \rho_f + \varepsilon_f) / \varepsilon_s) T_\infty^4 + \tau_f T_s^4 \quad (3.5)$$

Calibration was performed by measuring values of T_s with a thermocouple over a range of values of T_{ap} . To ensure the radiative properties of the polypropylene film did not change with time (due to possible contamination of its surface), calibration was performed before and after the measurement cycle, and to ensure consistency of these properties between locations, calibration was carried out at different points on the PCB surface.

Oil based heatsink was suggested for thermal mapping of microprocessor by [34]. The proposed setup measures processor temperature using an infrared camera. It captures the chip temperature with an infrared (IR) camera. An infrared transparent heatsink is used to allow the IR camera to obtain the processor die temperature. Figure 3.5 shows the measurement setup using this method.

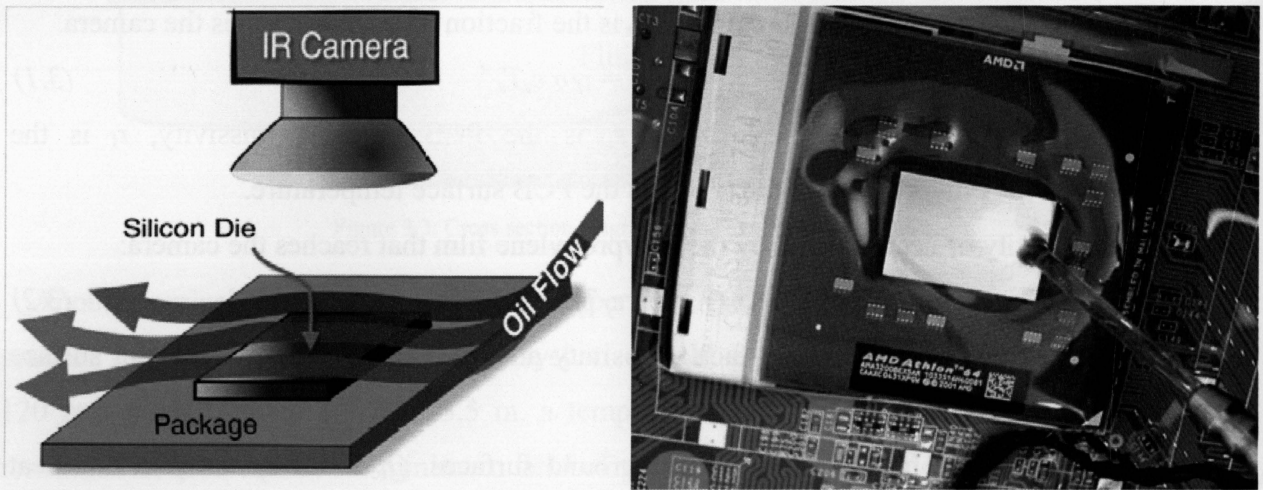


Figure 3.5: Measuring setup [34].

After considering most recent infrared thermography measurement setups, the method proposed by [34] was selected which is the most appropriate one according to our field of interest.

3.2 Proposed IR thermography setup

The major apparatus used in the proposed experimental setup include an FLIR infrared camera system, data acquisition system, digital thermometer, infrared transparent oil (Aldrich oil), oil pump and power supply. A typical measurement setup is shown in Fig. 3.6. The measurement setup is capable of capturing up to 420 frames per second (fps) with a $10\mu\text{m} \times 10\mu\text{m}$ spatial resolution, and it can be applied to multiple chips with relative simplicity. The IR camera frame rate can be increased up to 10 KHz as long as the bandwidth of the camera stays under 1GB/s. The equipment and instrumentation used to conduct the experimental measurement are discussed in this chapter.

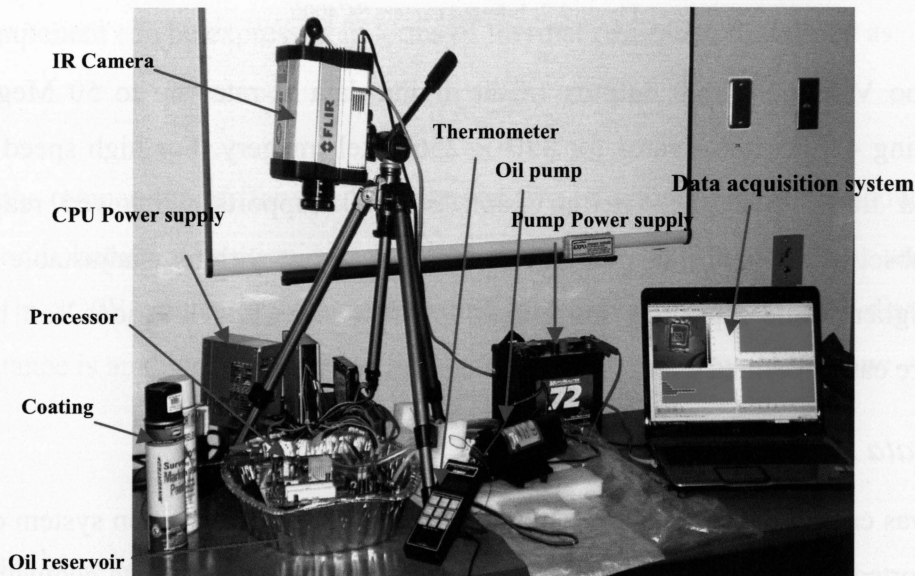


Figure 3.6: Typical measurement setup.

3.2.1 Infrared Camera

The infrared camera used in this measuring setup is a FLIR SC4000 camera (Fig. 3.7) which is a high-speed, high-resolution, high sensitivity, science-grade infrared camera with Gigabit Ethernet, Camera Link and USB interfaces for maximum flexibility and performance. With a 320×256 pixel Indium Antimonide (InSb) detector, the ThermoVision SC4000 camera offers unmatched resolution and thermal sensitivity. An extremely sensitive detector and high speed

read out design, provide the camera with extraordinary image quality for the most demanding applications.



Figure 3.7: Infrared camera SC4000.

The Thermo Vision SC4000 outputs 14-bit digital data at rates up to 50 Mega pixels per second, yielding 420Hz frame rates for 320×256 pixel imagery. For high speed applications and increased frame rates the ThermoVision SC4000 supports windowed readout modes, allowing a subset of the total image to be selectively read out with user-adjustable window size at a much higher frame rate. The sub-sample window sizes and locations can be arbitrarily chosen and are easily defined using the camera control software [51].

3.2.2 Data Acquisition System

The data was captured and analyzed using the integrated data acquisition system of the optical system, supported by PC-based ThermaCAM Researcher software for data acquisition, analysis and reporting. ThermaCAM Researcher software contains powerful measurement and analysis functions for extensive temperature analysis, including isotherms, line profiles, area histograms and image subtraction capability. The acquired input data were recorded in real time for subsequent analysis using this software package. Additionally the SC4000 camera system has an optional Software Development Kit (SDK) for custom programming and interfacing to the camera which is introduced in detail in Chapter 5.

3.2.3 Heatsink

A heatsink is a medium that enhances heat dissipation from a hot surface, usually the case of a heat generating component, to a cooler ambient, usually air. In most situations, heat transfers across the interface between the solid surface and the coolant air and the solid-air interface represents the greatest barrier for heat dissipation. A heatsink lowers this barrier mainly by increasing the surface area that is in direct contact with the coolant. This allows more heat to be dissipated and/or lowers the device operating temperature.

The primary purpose of a heatsink is to maintain the device temperature below the maximum allowable temperature specified by the device manufacturer [35]. Using temperatures and the rate of heat dissipation, a quantitative measure of heat transfer efficiency across two locations of a thermal component can be expressed in terms of thermal resistance R , defined as:

$$R = \frac{\Delta T}{Q} \quad (3.6)$$

where ΔT is the temperature difference between the two locations. Figure 3.8 shows the thermal resistance circuit between junction and ambient of a chip. The measurement unit of thermal resistance is in $^{\circ}\text{C}/\text{W}$, indicating the temperature rise per unit rate of heat dissipation. This thermal resistance is analogous to the electrical resistance R_e , given by Ohm's law:

$$R_e = \frac{\Delta V}{I} \quad (3.7)$$

with ΔV being the voltage difference and I the current.

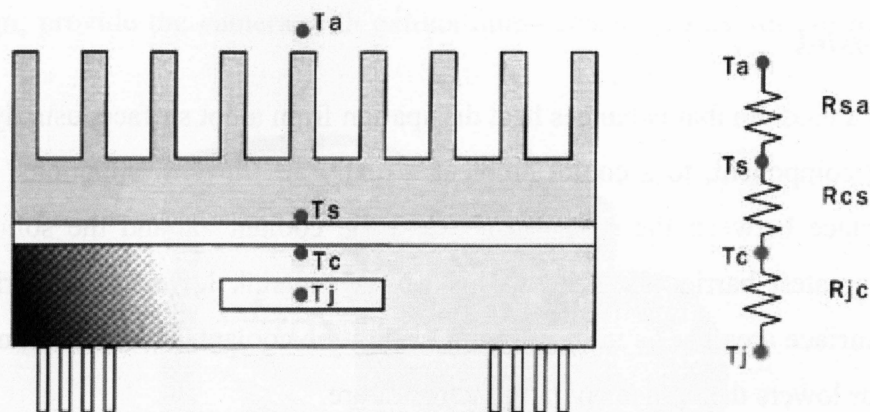


Figure 3.8: Thermal resistance circuit.

a) Heatsink Selection

One of the most important considerations in this measuring setup is to have the DUT operating in the conditions under which it was designed to operate. Under these conditions the cooling system of our DUT (a Dual Core processor) is a passive air cooling system which uses a fan with variable speed to remove the heat according to power dissipation.

The temperature distribution of the processor without a cooling fan is shown in Fig. 3.9. The thermocouple installed under the heatsink (LO1) indicates temperature of 52.3°C. However the heatsink is not transparent to IR radiation, therefore; the DUT temperature cannot be obtained directly.

Several liquids to act as coolants were explored in [34]. Water, which has a very high specific heat, makes it ideal for such experiments, but it is opaque to the IR camera. Several fluoride materials are extremely transparent to IR with a high capacity to cool down modern processors, but their toxic nature makes them unsuitable. The most transparent IR material was olive oil which was transparent enough to perform good measurement, but difficult to be pumped due to its high viscosity.

Aldrich Mineral Oil 161403 was selected as the heatsink for the test setup due to its elevated transparency in the infrared spectrum, high specific heat, relatively high thermal conductivity, relatively low viscosity, and chemical safety. The oil was pumped to the surface of the chip and is capable of removing 100W heat from the DUT.

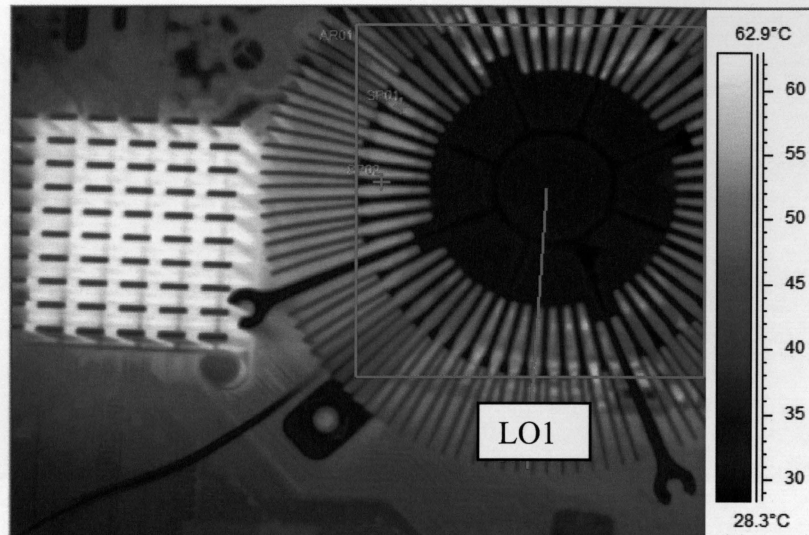


Figure 3.9: Temperature distribution of the processor with air cooling.

b) Heatsink Flow

The oil flow regime is a major factor affecting the temperature measurement of the DUT in the experimental setup. Several different oil flow scenarios were studied. Three important cases are reported as follow:

1) Turbulent flow: the oil pipe is positioned about 5 cm above the DUT and the oil was pumped directly to the surface of the DUT. The magnitude of the temperature versus time is represented in Fig. 3.10.

2) Turbulent flow at an angle of 45 degree: the oil pipe is positioned about 5 cm above the DUT, but the oil was pumped with 45 degree angle. The magnitude of the temperature versus time is represented in Fig. 3.11.

3) Laminar flow: oil flows over the DUT with almost angle of zero and in parallel layers. The magnitude of the temperature versus time is represented in Fig. 3.12.

The obtained results indicate that the turbulent flow in both Fig. 3.10 and Fig. 3.11 has more fluctuation in temperature than laminar flow shown in Fig 3.12. Since the obtained results of turbulent flow were unstable, laminar oil flow regime was chosen as the heatsink system.

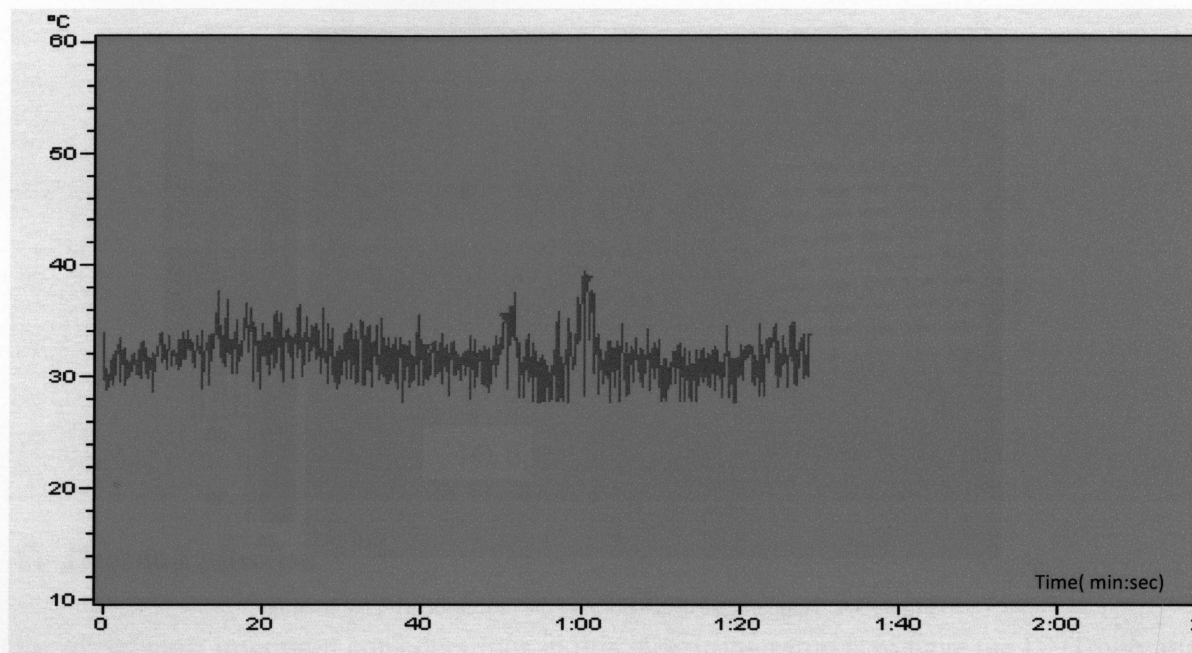


Figure 3.10: Temperature measurement with turbulent oil flow.

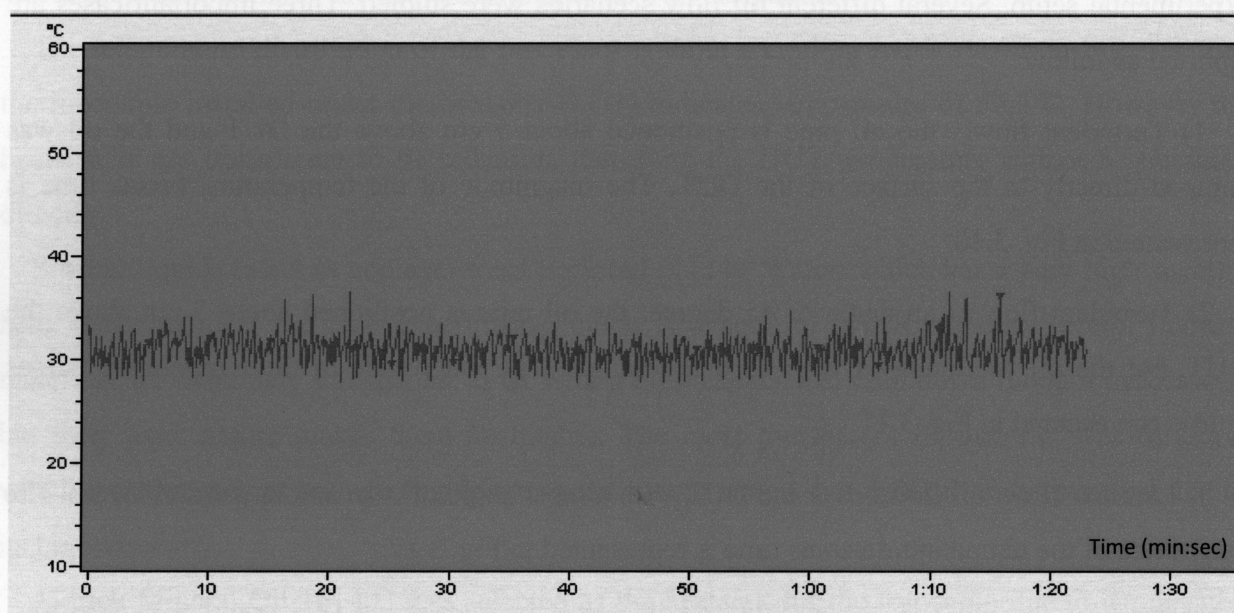


Figure 3.11: Temperature measurement with turbulent oil flow at an angle of 45°.

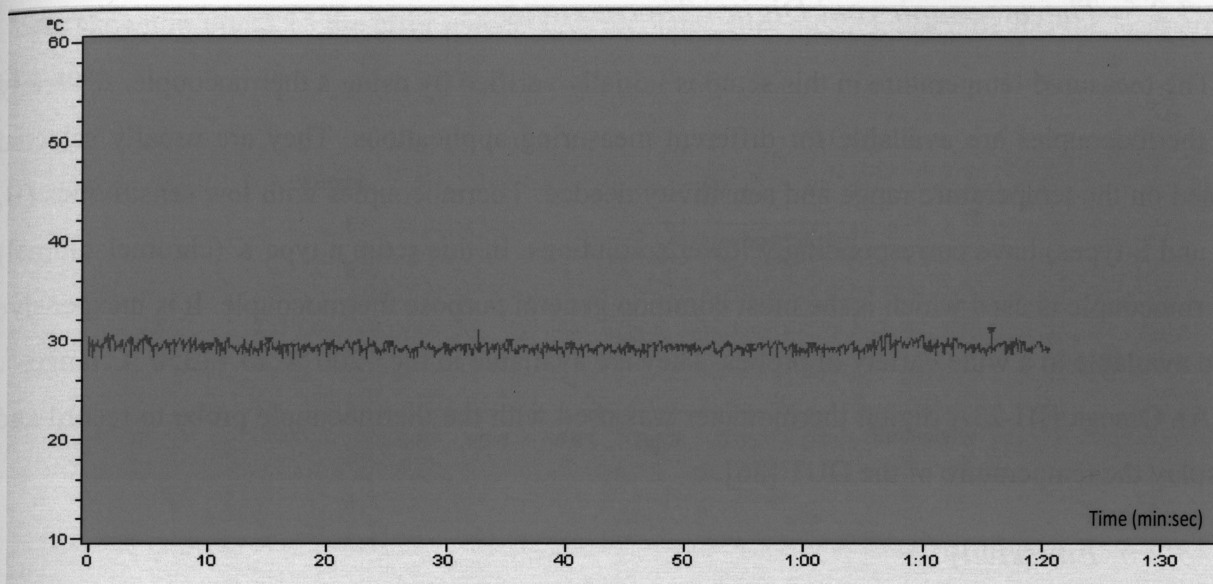


Figure 3.12: Temperature measurement with laminar oil flow.

3.2.4 Oil Pump

The utility pump shown in the Fig.3.13 is suitable for variety of tasks such as pumping mineral oil [7] since it is designed especially for harsh fluid transfer. A 12V DC battery was used to power the pump.

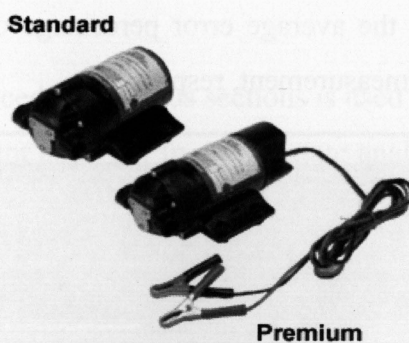


Figure 3.13: Utility pump.

3.2.5 Thermocouple and Digital Thermometer

The measured temperature in this setup is initially verified by using a thermocouple. A variety of thermocouples are available for different measuring applications. They are usually selected based on the temperature range and sensitivity needed. Thermocouples with low sensitivities (B, R, and S types) have correspondingly lower resolutions. In this setup a type K (chromel–alumel) thermocouple is used which is the most common general purpose thermocouple. It is inexpensive and available in a wide variety of probes. They are available in the $-200\text{ }^{\circ}\text{C}$ to $+1350\text{ }^{\circ}\text{C}$ range.

An Omega HH-23A digital thermometer was used with the thermocouple probe to record and display the temperature of the DUT [36].

3.2.6 Emissivity

One of the most important parameters that affect the temperature measurement of the DUT is emissivity. As described previously it defines the fraction of radiation emitted by an object as compared with emitted by a perfect radiator (blackbody). Emissivity value is between 0 and 1 and depends on the material of the object, surface condition (surfacing method, geometry), the temperature of the object, wavelength, and direction of radiation.

The default emissivity of camera is set to 0.92; however the real emissivity might be different from this value. Figures 3.14 and 3.15 illustrate the temperature measurement of the DUT using different emissivity values and the average error percentage of IR thermography measurement with reference to thermocouple measurement, respectively.

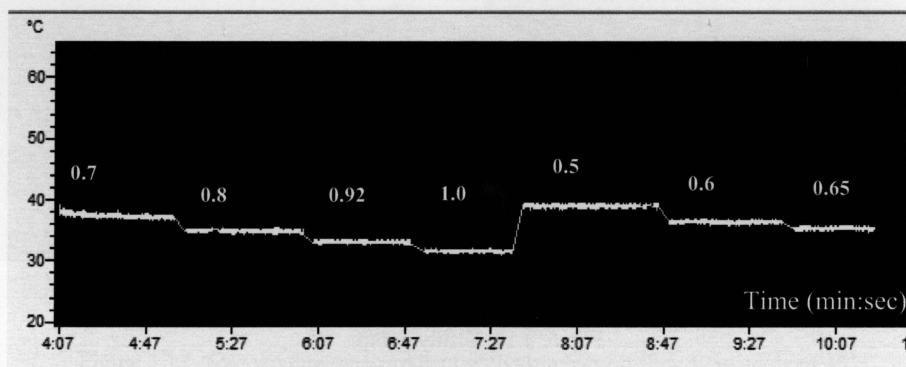


Figure 3.14: Emissivity effect on temperature measurement of the DUT.

As shown in Fig. 3.15 the error percentage calculated for emissivity of 0.61 has the least error of 1.09%.

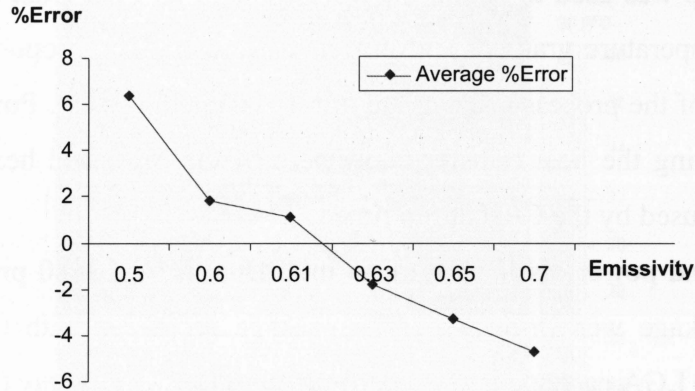


Figure 3.15: Percent error with emissivity from 0.5 to 0.7.

Another way to create a uniform surface emissivity and increase the accuracy of the measurement is covering the surface of DUT by special coating with known emissivity. Boron nitride spray and black paint are suitable for PCB and electronic devices; however in our experimental setup we didn't use them and measured the emissivity.

3.2.7 Type of Analysis

The measurement setup introduced in previous sections is used to perform two type of analysis a) steady state analysis, b) transient analysis. In steady state analysis, after switching the power ON, a time interval is given to the system to reach its steady state condition. It is due to the fact that oil based heatsink takes some period of time to completely cover the whole surface of the DUT and remove the heat homogenously.

To perform transient analysis on the DUT, an abnormal stress is imposed to a system. This can be in the form of changing ambient temperature, different load condition, changing cooling speed, etc. In this work a standard benchmark was used to test the DUT in different workload condition.

3.3 Thermal Analysis of an Intel Dual Core E2180 Processor

The proposed setup was used to obtain the test results of an Intel Dual Core E2180 processor [38] in terms of temperature gradient and power dissipation. The proposed setup provides the temperature profile of the processor using the infrared camera system. Power dissipation data is obtained by calculating the heat transfer coefficient of the oil based heatsink and verified by isolating the current used by the CPU at run time.

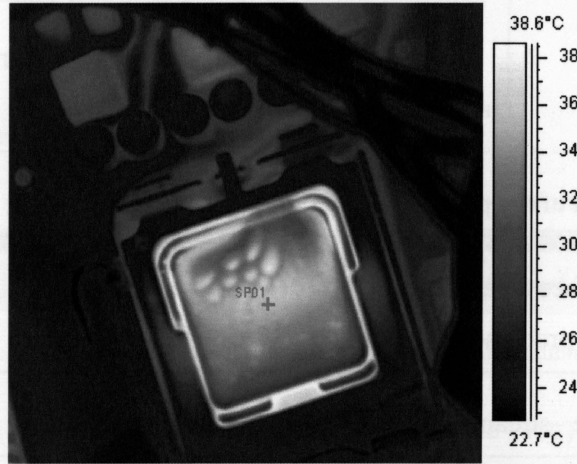
The temperature and power dissipation of an Intel Dual Core E2180 processor packaged in a 775-Land LGA package were measured. The package interfaces with the motherboard via a LGA775 socket. The LGA package is a standard flip chip Ball Grid Array (BGA) shipped with no sphere. The processor has an integrated heat spreader (IHS) whose main function is to transfer the non-uniform heat distribution from the die to the top of the IHS, out of which the heat flux is more uniform and spread over a larger surface area. The amount of power that can be dissipated as heat through the processor package substrate and into the socket is usually minimal.

3.3.1 Temperature Measurement

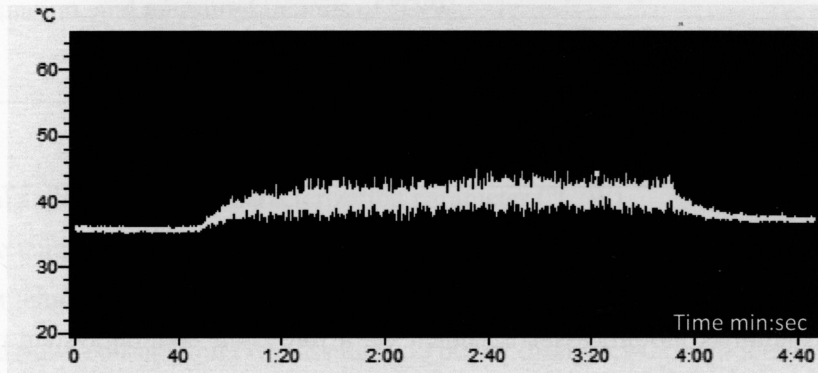
The temperature profile of the processor during transient condition was obtained using the proposed setup. After the system reached its steady state condition, transient analysis of the system was performed by running SPEC CPU 2006 version 1.1 [46] benchmark. The benchmark is an industry-standardized, CPU-intensive benchmark suite, stressing a system's processor, memory subsystem and compiler. It has been designed to provide a comparative measure of compute-intensive performance across the widest practical range of hardware using workloads developed from real user applications.

By running the benchmark, the temperature of the DUT increased from 36°C to maximum 44.8 °C. The different components of the benchmark were run for a time period of 3 minutes. After stopping the benchmark, the temperature decreased in less than 10 seconds and reached its steady state condition. The 2D temperature profile at $t=57s$ and temperature evolution of SP01 location (spot 1 which is a hot spot on the processor surface) versus time of the processor running the benchmark components are shown in Fig. 3.16 (a) and (b), respectively. The cooling system

was sufficient enough to remove the heat and control the temperature distribution over the processor.



(a)



(b)

Figure 3.16: Transient analysis of the processor, (a) 2D temperature profile at $t=57s$, (b) temperature evolution of SP01 location versus time.

3.3.2 Power Measurements

To measure the power dissipation and power consumption of the processor two approaches were used. The first approach consists of power dissipation measurement by calculating the heat transfer coefficient of the heatsink whereas in second approach the power consumption was calculated by measuring the current flowing through the processor

a) First Approach

The processor is cooled by a forced convection cooling system using a mineral oil as coolant and an oil pump. The specifications of the oil and pump are listed in Table 3.1.

TABLE 3.1: SPECIFICATION OF THE COOLING SYSTEM

Length of the processor	5 cm
Surface area of the processor	25 cm ²
Oil free –stream velocity	0.4m/s
Oil viscosity	0.013-0.015 kg/m.s
Oil density	838 kg/m ³
Oil specific heat	1.67 kJ/kg.°K
Oil thermal conductivity	0.138 W/m.°K

Under typical conditions the processor is cooled via a forced air cooling system using an aluminum heatsink and attached fan. The heatsink is attached to the integrated heat spreader (IHS) by a thermal interface material (TIM) as shown in Fig. 3.17.

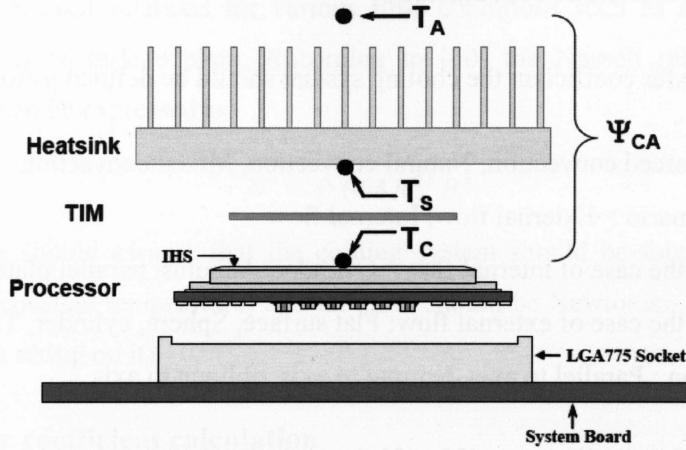


Figure 3.17: Processor thermal characterization parameter relationships.

The case-to-local ambient thermal characterization parameter value (Ψ_{CA}) is used as a measure of the thermal performance of the overall thermal solution that is attached to the processor package. It is defined by the following equation, and measured in units of $^{\circ}\text{C}/\text{W}$:

$$\Psi_{CA} = (T_C - T_A) / P_D \quad (3.8)$$

Where:

Ψ_{CA} = Case-to-local ambient thermal characterization parameter ($^{\circ}\text{C}/\text{W}$)

T_C = Processor case temperature ($^{\circ}\text{C}$)

T_A = Local ambient temperature in chassis at processor ($^{\circ}\text{C}$)

P_D = Processor total power dissipation (W) (assumes all power dissipates through the IHS) [38]

The case-to-local ambient thermal characterization parameter of the processor, Ψ_{CA} , is comprised of Ψ_{CS} , the thermal interface material thermal characterization parameter, and of Ψ_{SA} , the sink-to-local ambient thermal characterization parameter:

$$\Psi_{CA} = \Psi_{CS} + \Psi_{SA} \quad (3.9)$$

The interface material, aluminum heatsink and its fan have been replaced by a transparent oil heatsink which dissipates the heat by forced convection cooling method. It was assumed that all power dissipates through the IHS [38] and the heat transfer by conduction through ball contacts is neglected. Therefore, to calculate the heat flux (power) one needs to measure the heat transfer coefficient of the convection cooling system.

1) Heat transfer coefficient correlations

To calculate the heat transfer coefficient the cooling system should be defined as follow [39]:

- Flow scenario: Forced convection, Natural convection, Mixed convection
- Flow domain scenario : External flow, Internal flow
- The geometry in the case of internal flow: Cylinder, Annulus, parallel plate ,duct
- The geometry in the case of external flow: Flat surface, Sphere, cylinder, Tube bank, Packed bed,
- The flow direction : Parallel to axis, Normal to axis, oblique to axis

There are different equations in literature [39- 42] for various conditions in forced convection. They are based on the Dittus–Boelter heat transfer correlation for fluids. These equations can be expressed as follows:

$$h = \left(\frac{k}{l} \right) N_u \quad (3.10)$$

where k is the thermal conductivity of the liquid, l is hydraulic diameter, length of the plate (in this study) and N_u is the Nusselt number. The Nusselt number is a function of Prandtl number which is the ratio of momentum diffusivity and thermal diffusivity and Reynolds number .This number is the ratio of inertia force to viscous force.

$$Pr = \text{Prandtl number} = \frac{\nu}{\alpha} = \mu \frac{C_p}{k} \quad (3.11)$$

$$Re = \text{Reynolds -number} = V \frac{l}{\nu} = \rho V \frac{l}{\mu} \quad (3.12)$$

where:

$$\nu = \frac{\mu}{\rho} = \text{Kinematic viscosity (m}^2/\text{s)}$$

$$\alpha = \frac{k}{(\rho C_p)} = \text{Thermal diffusivity (m}^2/\text{s)}$$

$$\mu = \text{Viscosity (pa. s)}, \rho = \text{Density (kg/m}^3), C_p = \text{Specific heat (J/kg.k)}, V = \text{Fluid velocity (m/s)}$$

There are different Nusselt relations for various flow conditions such as internal, external, over a vertical plate or horizontal surface plate. According to [40] the Nusselt relation which applies for horizontal flat surface can be expressed as:

$$N_u = 0.664 R_e^{0.5} P_r^{\frac{1}{3}} \quad (3.13)$$

To use Eq. (3.13) one should assume that the cooling system should be forced convection, the plate should be isothermal (constant temperature) and the fluid should be Newtonian, (fluid continues to flow, regardless of the forces acting on it).

2) Heat transfer coefficient calculation

By using the specification of the oil, pump and processor, listed in Table 3.1, the Prandtl number, Reynolds number and finally Nusselt number can be calculated according to the Eqs. (3.11), (3.12), and (3.13) as follows:

- Re: 1420
- Pr. : 157
- Nu. : 135

By substituting the cooling system specification in Eq. (3.10), the heat transfer coefficient of **339 W/m².K** was obtained.

3) Heat transfer coefficient measurement

To measure the heat transfer coefficient, a 50 Ω power resistor was installed over a circuit board and connected to a DC power supply. By increasing the voltage, the power dissipation of the resistor was increased and its case temperature profile was measured using the IR camera. By considering the applied voltage, power dissipation of the resistor ($P_D = V^2/R$), ambient temperature (23 °C) and case temperature profile of the resistor, a formula according to Eq. (3.8) was included in the “Formula” section of the IR camera software to measure the case to ambient thermal resistance.

The power dissipation of the 50 Ω resistor increased from 4.5W to 32W as shown in Fig. 3.18 and the thermal resistance was plotted according to different powers versus time.

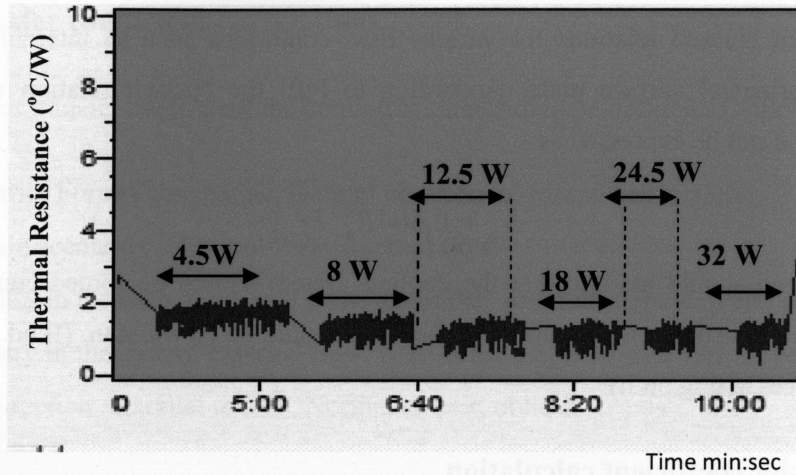


Figure 3.18: Thermal resistance for various power dissipations.

The average thermal resistance versus power is shown in Fig. 3.19.

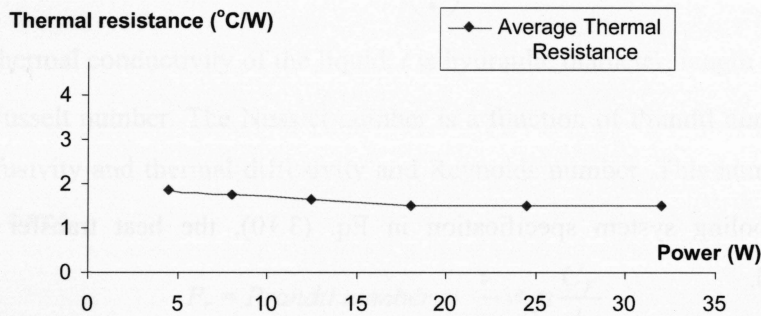


Figure 3.19: Average thermal resistance.

It can be seen that the thermal resistance reaches a constant value as the power dissipation increases. By considering the average thermal resistance of 1.5°C/W and surface area of the resistor (19cm^2), the heat transfer coefficient of $350\text{ W/m}^2\cdot\text{K}$ ($h = 1/R.A$) can be obtained. In this case the average error between measurement and calculation is 3.5%. The obtained heat transfer coefficient by resistor ($350\text{ W/m}^2\cdot\text{K}$) was used to calculate the power dissipation of the processor.

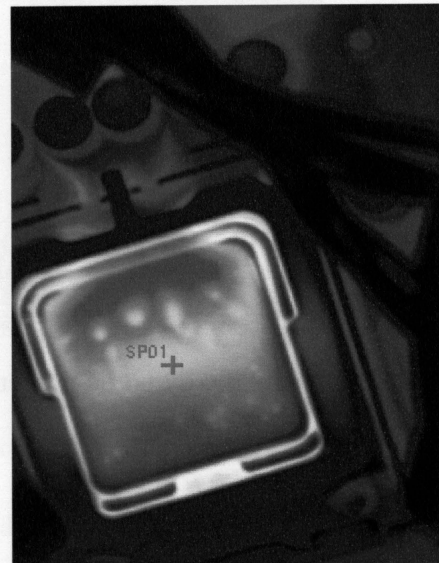
The processor workload was changed from idle mode to load condition by performing the SPEC CPU2006 benchmark. The sequential views of the temperature profiles obtained from this

test are shown in the Fig. 3.20 (a)-(d). It can be seen that the temperature of the SP01 (spot 1 which is a hot spot on the processor surface) increases from 36.7°C to 38.3°C, 42.3°C and 44.8°C, respectively.

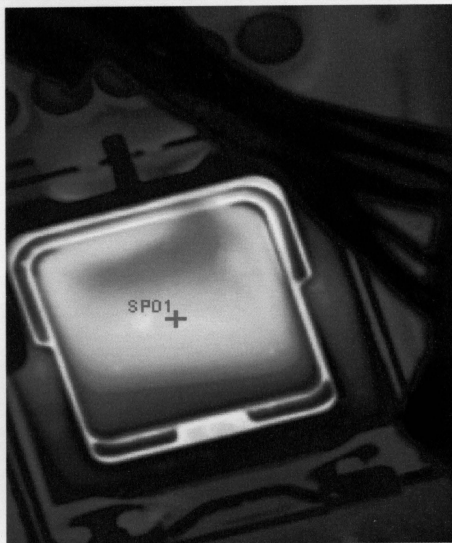
The power dissipation curve versus time obtained from the test is shown in Fig. 3.21. It can be seen that dissipated power changed from 5.5W in steady state mode to maximum of 18W under loading condition. In addition, it can be observed that the fluctuation of the power dissipation under loading condition is much more than steady state mode due to running different programs and therefore increasing the dynamic power dissipation.



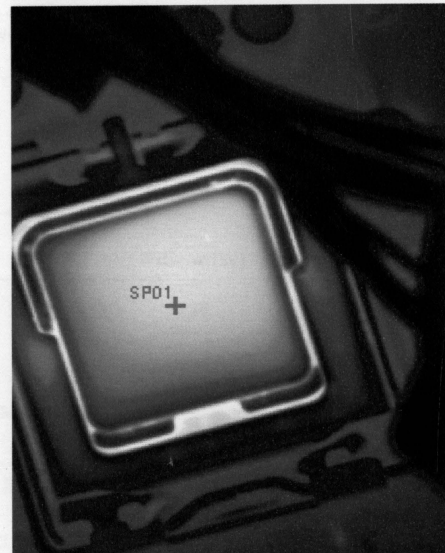
(a)



(b)



(c)



(d)

Figure 3.20: Temperature profile at (a) $t=32$ sec. (b) $t=41$ sec. (c) $t=60$ sec. (d) $t=73$ sec. while running the benchmark.

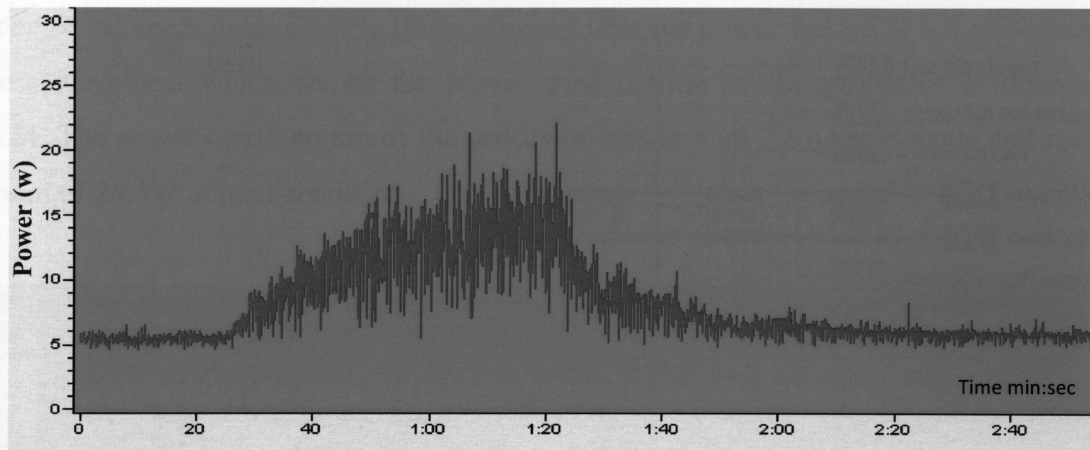


Figure 3.21: Power dissipation curve versus time.

b) Second Approach

The main power lines for the processor operate at 12V, and then are fed to a voltage regulator (VR) module, which converts this voltage to the actual processor operating voltage and provides tight control on voltage variations. Therefore, the power was measured as follow:

- 1- The current of the power lines for the processor was measured by a Fluke 80i current probe which has two output conversion of 10mV/A and 100mV/A.
- 2- The output of the current probe was read by a Fluke 45 digital multi meter (DMM) which has a pc interface via RS232 serial port.
- 3- Labview version 8.5 was used for data acquisition (DAQ) and DMM control. A program was written by its programming language “G” to read the output of the DMM and calculate the power consumption of the processor. The program and waveform of the power are shown in Fig. 3.22 and Fig. 3.23, respectively.

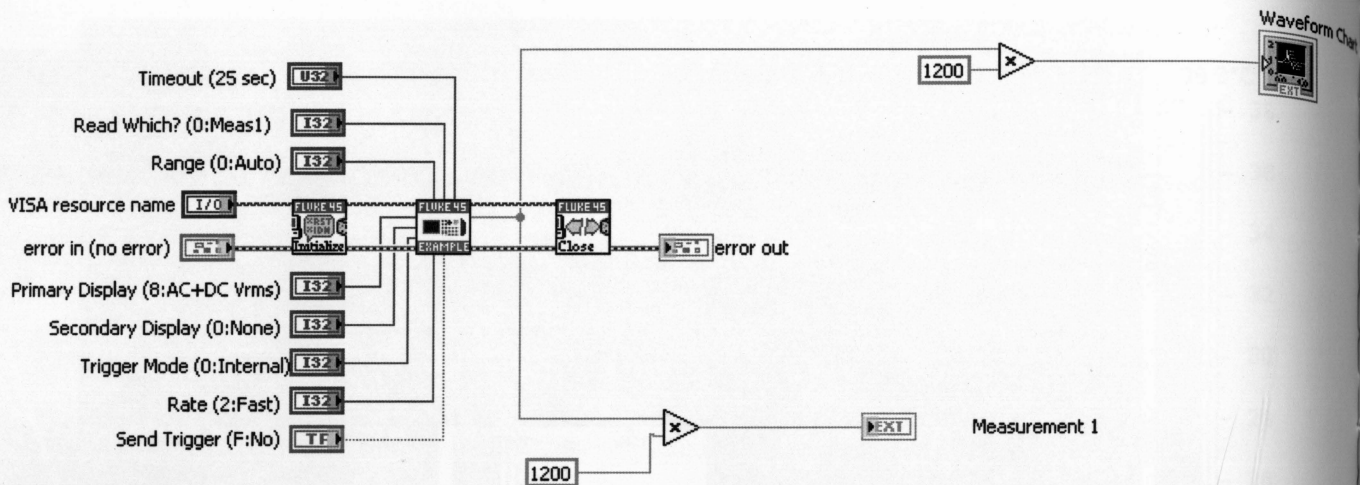


Figure 3.22: Labview interface with DMM.

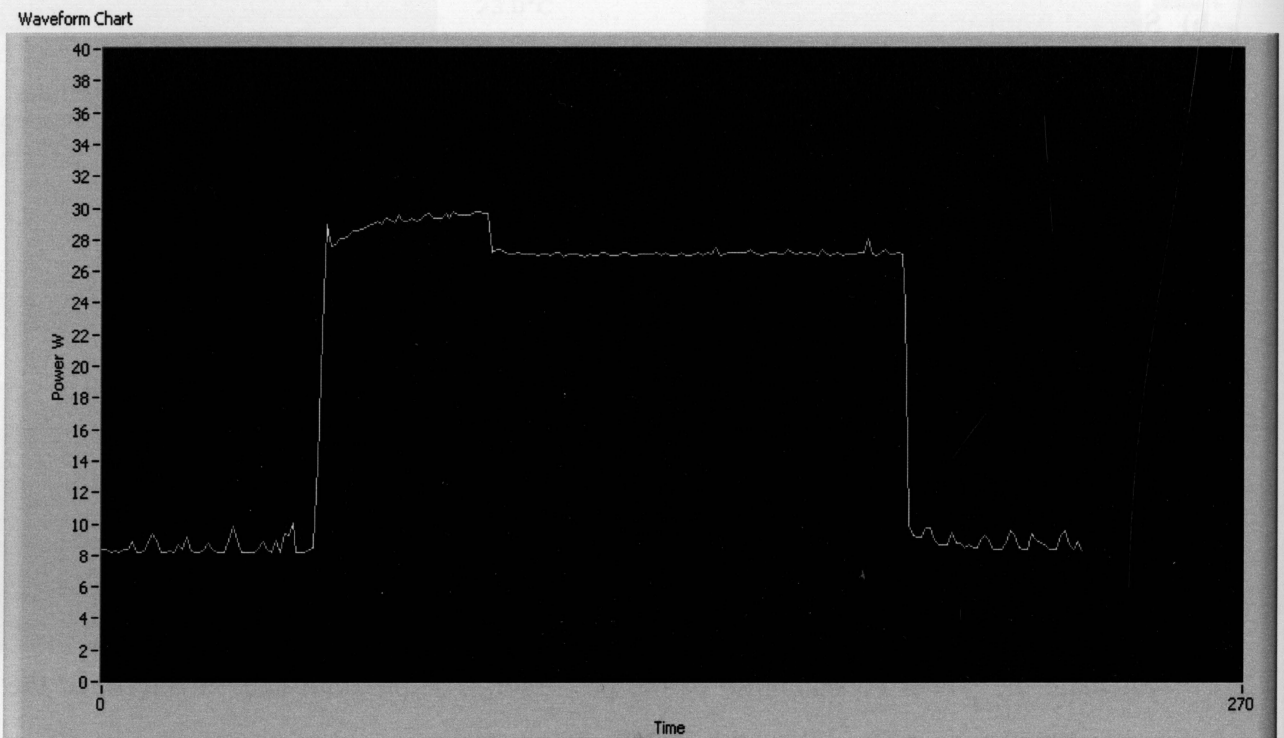


Figure 3.23: Total power consumption waveform.

The waveform in Fig. 3.23 is related to the power consumption of the processor and its voltage regulator circuit when it goes from idle mode to executing the Spec CPU2006 with rate of 5 samples per second. The power increased from 8.5W in idle mode to 30 W (load condition) and after stopping the benchmark it decreased to 8.5 W.

Since the voltage regulator is not 100% efficient then the power wasted in VR was discounted and new waveform which shows the power consumption of the processor is illustrated in Fig. 3.24. The power consumption of the processor was around 7W in idle mode and reached a maximum of 24.5W at load condition.

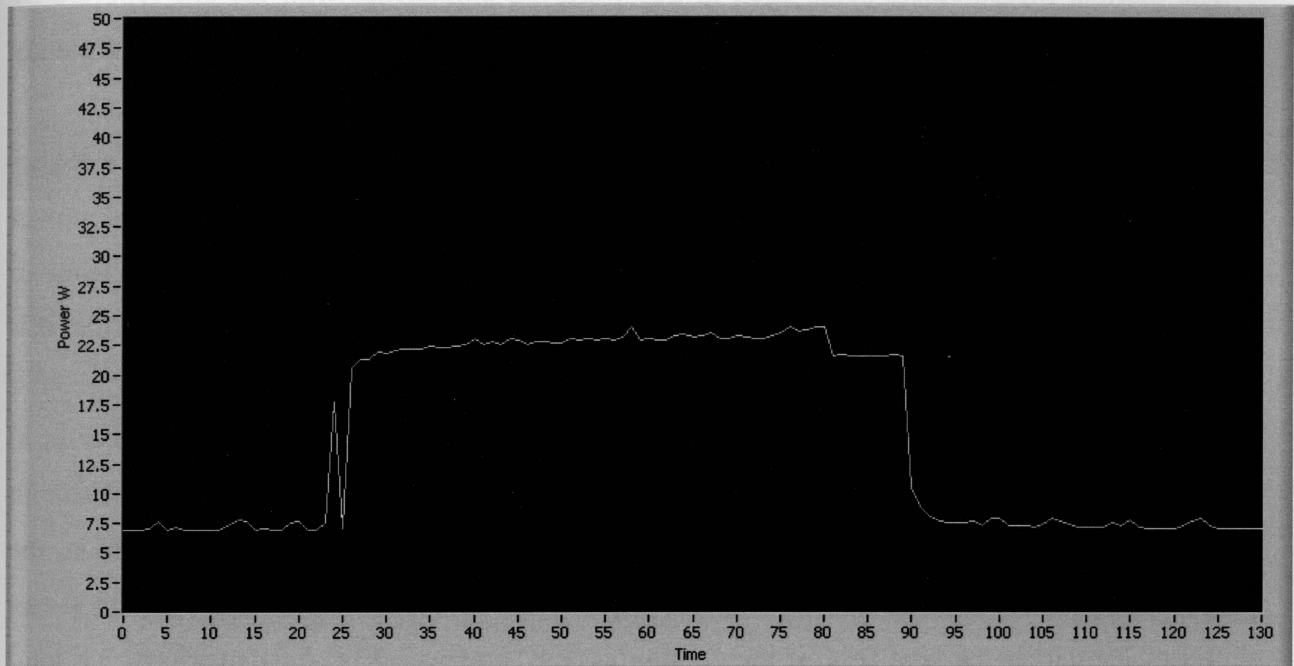


Figure 3.24: Power consumption of the processor during load condition.

3.4 Discussion

In the first approach the power dissipation of the processor was measured by IR thermography while running the SPEC CPU2006 benchmark. The two main sources of power dissipation in the microprocessor are static power, which results from resistive paths between power supply and ground, and dynamic power, which results from switching capacitive loads between different voltage levels. There is a third source of power dissipation in CMOS circuits, short-circuit current, which results from both transistors in a CMOS circuit being on at the same time while the input switches, however the short-circuit component is small and negligible [57].

At the same time of measuring the power dissipation by IR thermography, the total power consumption of the processor was measured according to the method described in second

approach. The results showed that around 80% of the total power consumption was dissipated as heat. Since the power dissipated in a CMOS circuit accounts for more than 75% of the power consumption for recent technologies [53], the obtained results are satisfactory.

3.5 Comparison With Existing Work

The thermal measurement setup used in this work has similarities with the one reported by Hamann et al [58]. The key difference is that their setup only performs measurements for steady state thermal analysis; therefore, the evolution of power cannot be captured.

Isici et al [4] measured the overall power consumption with a multimeter and used a logger machine to collect the power data. A significant difference between the proposed power measurement setup and [4] is that the proposed approach also takes into account the efficiency of the on-board voltage regulator to increase the accuracy. The main difference is the fact that this setup also captures the temperature profile of the DUT.

The proposed thermal measurement setup is similar to the setup described by Martinez et al [34]. However a major difference is the use of a clamp ammeter instead of a shunt resistor to avoid the need to cut the power supply lines and add more wires to the system. In addition, the proposed approach converts the temperature profile of the device to its power dissipation at run time by calculating the heat flux of the cooling system, however; [34] only measures the total power consumption of the device under test.

3.6 Summary

Different setups developed for infrared thermography by researchers were introduced and their advantages and drawbacks were discussed. Infrared thermography setup based on "Oil heatsink" was selected for this research.

The IR thermography measurement setup to obtain the temperature profile and power dissipation of a modern high performance processor was discussed. The major equipments and the systems used in the experiment setup were discussed in detail in this chapter. The effect of various parameters such as the oil flow condition and emissivity of the target were studied and the proposed setup for this research work was discussed.

The measurement setup was used to obtain the temperature profile and power dissipation of the processor while running the SPEC CPU2006 benchmark. Power dissipation of the processor was measured by calculating the heat transfer coefficient of the heatsink and verified by measuring the total power consumption of the processor at the same time. The results showed that around 80% of the total power consumption was dissipated as thermal energy (heat).

Chapter 4

THERMAL MODEL OF THE INTEL DUAL CORE E2180 PROCESSOR

In this chapter the proposed measurement setup is used to verify the thermal model of an Intel Dual Core E2180 processor. The processor was modeled by COMSOL 3.4 [45] which is based on finite element method. This software is able to perform 3D transient and steady state thermal analysis and post process the output data, such as temperature distribution, in a 3D domain. The simulation results are compared to the experimental results obtained in Chapter 3.

4. Thermal Model of the Intel Dual Core E2180 Processor

The processor was an Intel Dual Core E2180 processor packaged in a 775-Land LGA package (see Fig. 4.1) that interfaces with the motherboard via a LGA775 socket as discussed in section 4.1. In this type of processor there are no additional components, such as BSRAMs, which generate heat on this package; therefore; amount of power that can be dissipated as heat through the processor package substrate and into the socket is usually minimal.

4.1 Finite Element Model

The processor, socket and its contact balls were modeled using COMSOL 3.4 finite element software. Since processor is Dual Core, two cores with total surface area of 111 mm^2 were

considered as heat sources with variable power consumption from zero to 65 W (Maximum thermal guideline of the processor [43]).

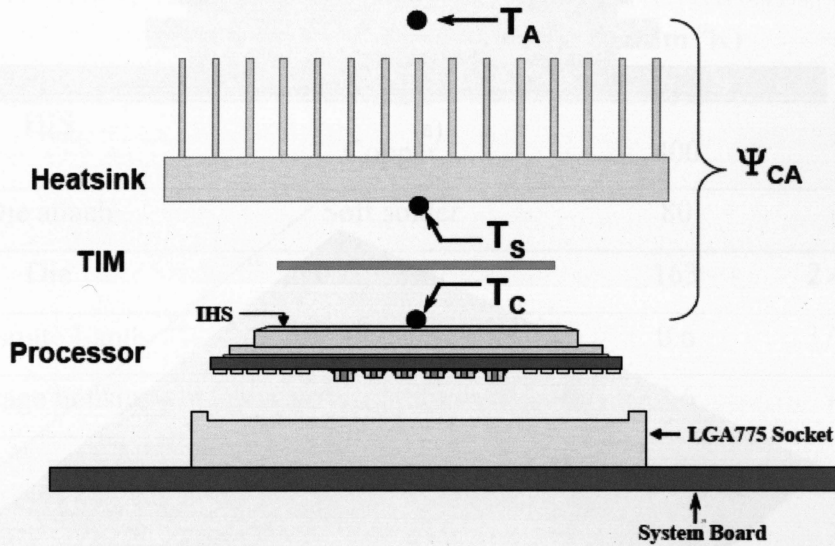
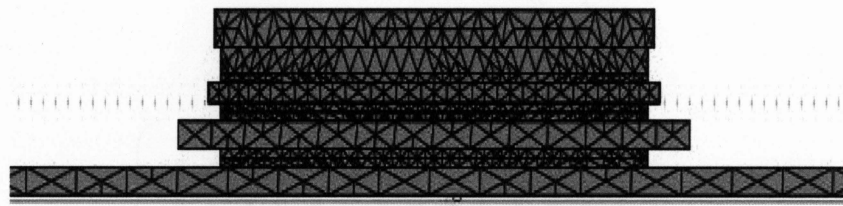


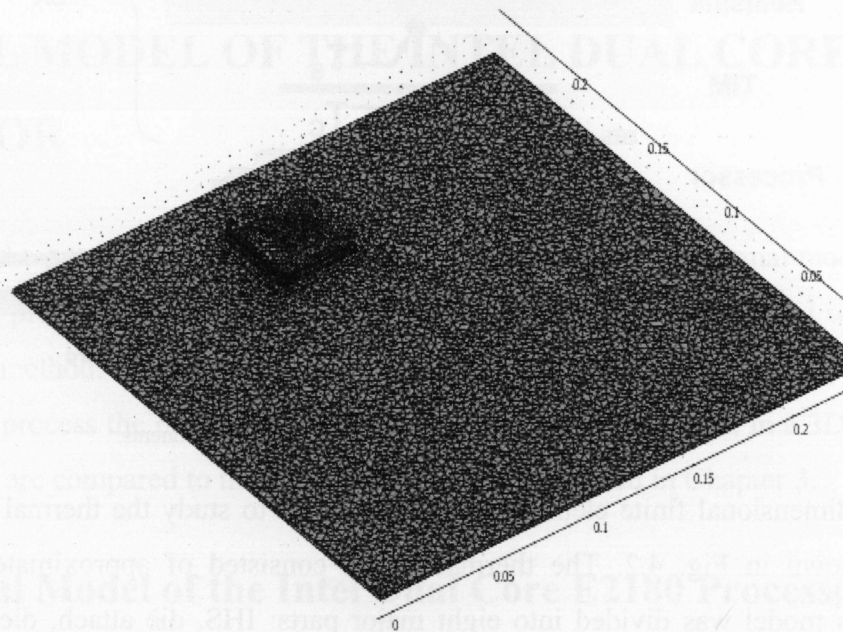
Figure 4.1: LGA 775 socket with its processor components.

The three dimensional finite element model developed to study the thermal properties of the package is shown in Fig. 4.2. The thermal model consisted of approximately 410000 solid elements. This model was divided into eight major parts: IHS, die attach, die, substrate lands, package housing, contact, solder and PCB [38].

Figure 4.2 shows the developed finite element model of the processor installed on the PCB which is an FR4 PCB with three copper layers. The material properties and dimensions of each layer are listed in Table 4.1.



(a)



(b)

Figure 4.2: Finite element model (a) 2D, side view ; (b) 3D view .

TABLE 4.1: MATERIAL PROPERTIES AND DIMENTIONS OF LAYERS OF THE THERMAL MODEL OF THE LGA PROCESSOR AND ITS SOCKETS.

Layer	Material	Thermal Conductivity (W/m °K)	Top view Dimension (mm)
HIS	Nickel	90.7	36 × 36
	Copper	400	
Die attach	Soft solder	80	10 × 11
Die	Silicon	163	2 × (5 × 11)
Substrate Lands	Reinforced resin	0.6	37.5 × 37.5
Package housing	Plastic mold	0.6	42 × 42
Contact	Copper	400	35 × 35
	Gold	317	
	Nickel	90.7	
Solder	Gold	317	35 × 35
	Copper	400	
PCB	FR4	0.3	240 × 240
	Copper	400	

4.2 Boundary and Subdomain Settings

The governing heat transfer equation is:

$$Q = \nabla \cdot (-k \nabla T) = h(T_s - T) \quad (4.1)$$

where Q (W/m³) is heat source, h is the heat transfer coefficient (W/m².k), T_s denotes the surface temperature (°C) and k is the thermal conductivity (W/m.k).

The boundary conditions were set as follows:

- The top layer of the board was considered as an insulator since under actual operating conditions this layer is filled by components.
- For the bottom layer of the PCB and sidewalls, heat flux was considered with a heat transfer coefficient of $10 \text{ W/m}^2\cdot\text{K}$ [44].
- For the top layer and sidewalls of the processor, heat flux was considered according to Eq. (4.1). The measurement results obtained in Chapter 3, including power dissipation and heat transfer coefficient were used to solve the boundary condition of this part. In Eq. (4.1), the power dissipation of the processor was considered as a heat source with ambient temperature of 23°C , and the obtained heat transfer coefficient was used for h .

4.3 Simulation Results

The numerical simulation was performed by applying the above-mentioned boundary conditions. Figures 4.3 and 4.4 show the simulation results for power dissipation of 5.5W and 18W, respectively with heat transfer coefficient of $350 \text{ W/m}^2\cdot\text{K}$ in ambient temperature of 23°C . The maximum case temperature of the model at power dissipation of 5.5W and 18W was obtained as 37.51°C and 46.25°C respectively which are in good agreement with the temperature profile of the processor obtained in Chapter 3. The IR thermography showed average temperature of 36°C for power dissipation of 5.5W and 44°C for power dissipation of 18W. There was good correlation between the temperature profile obtained from test results and finite element simulation.

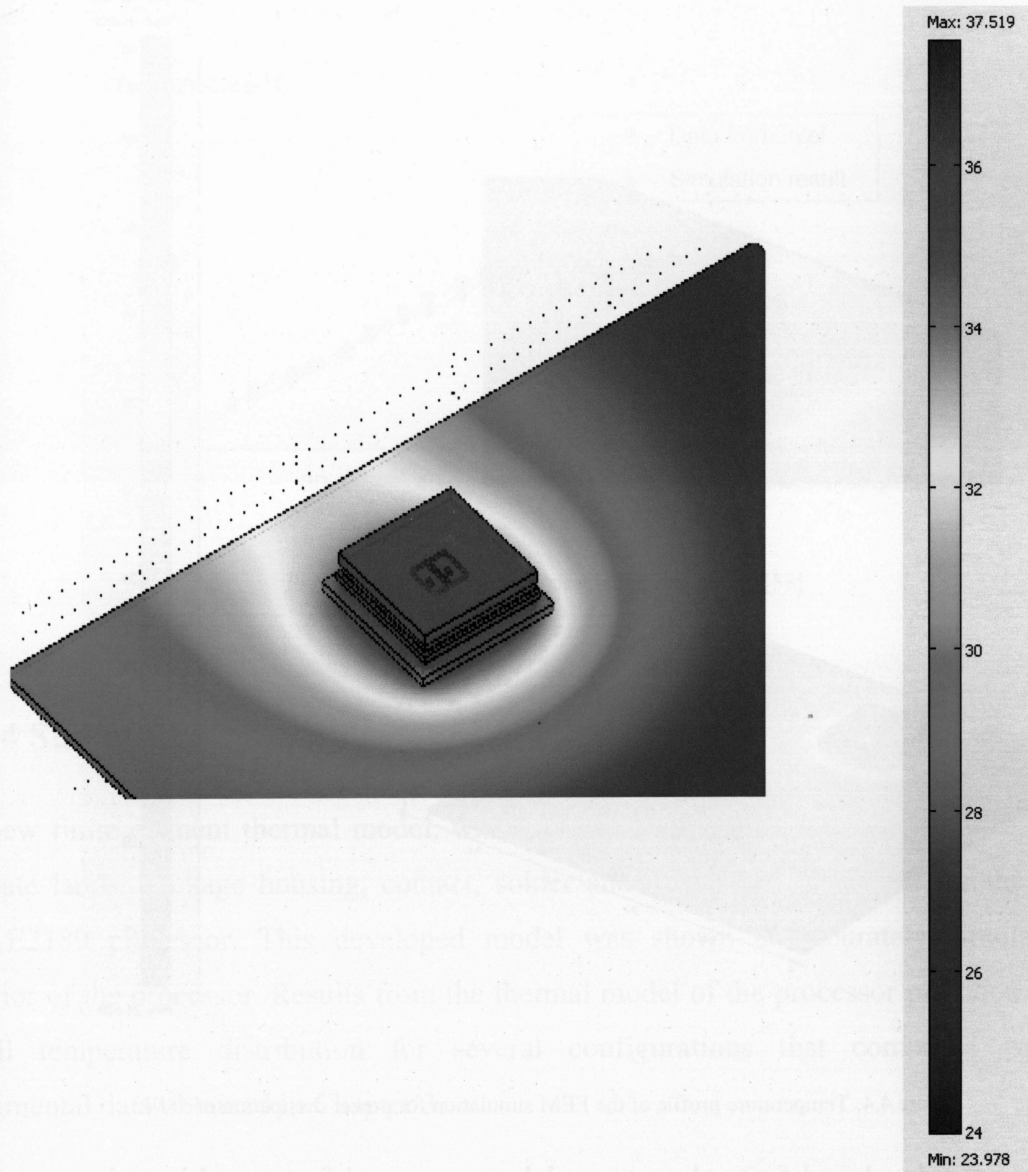


Figure 4.3: Temperature profile of the FEM simulation for power dissipation of 5.5W.

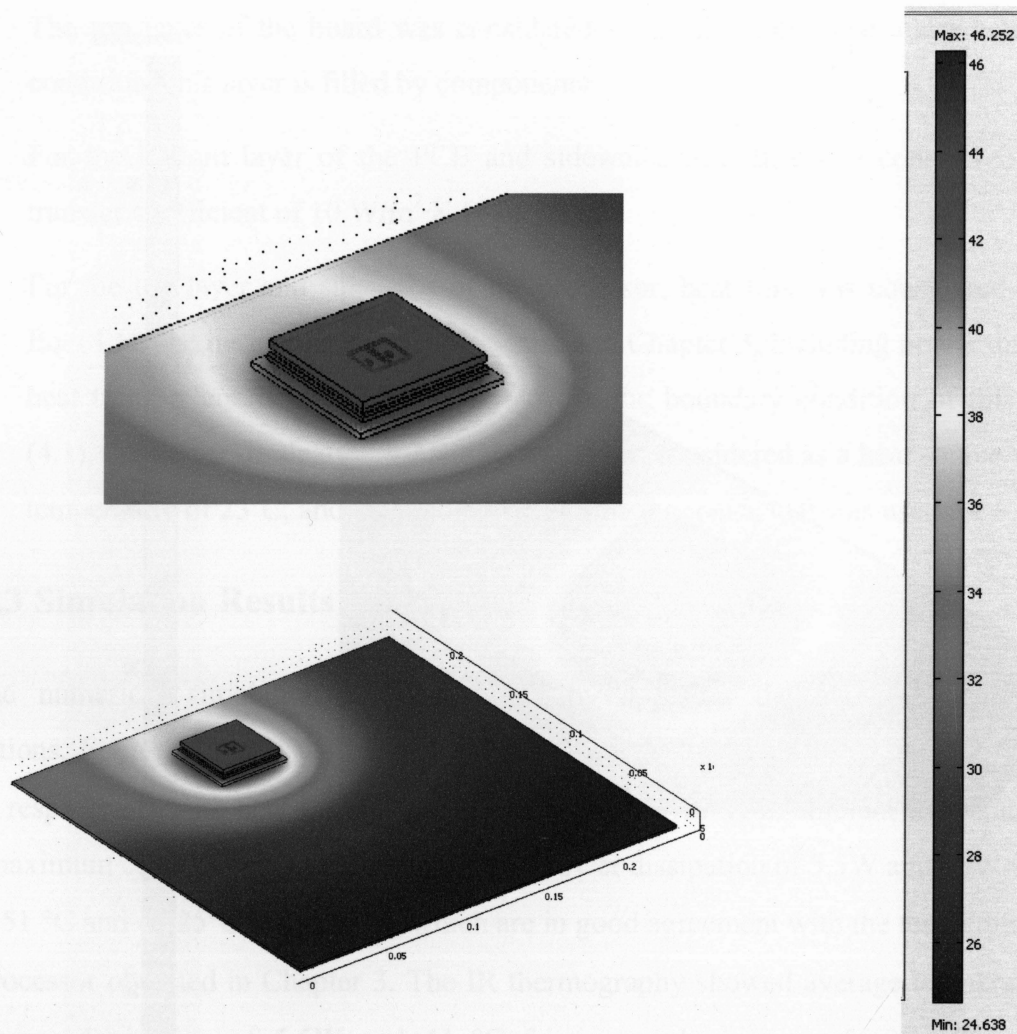


Figure 4.4: Temperature profile of the FEM simulation for power dissipation of 18W.

In addition, the developed finite element model was assessed for several boundary conditions scenarios, i.e. various heat transfer coefficients, according to Intel documentation for the processor [38]. The power dissipation was varied from 6 W to 65 W according to the thermal profile of the processor in its data sheet. The evolution of obtained temperature at the center of the processor from simulation results and [38] is shown in Fig. 4.5. It can be observed that the maximum error percentage is around 2.7%

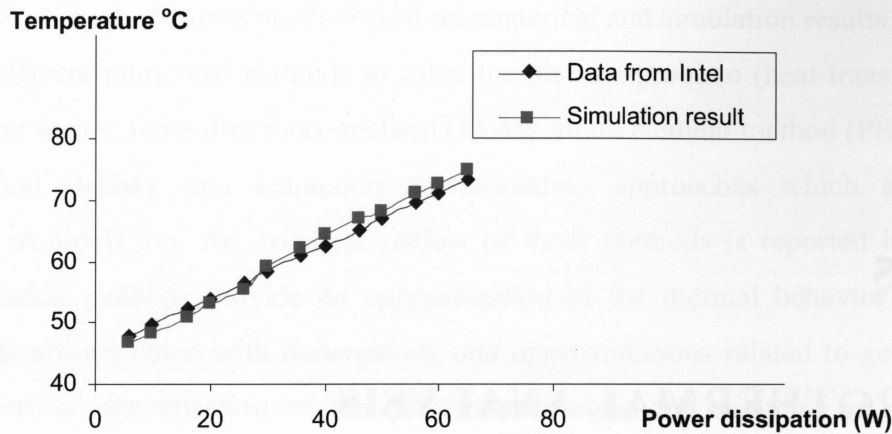


Figure 4.5: Comparison of simulation results and [38].

4.4 Summary

A new finite element thermal model, which included eight major parts: IHS, die attach, die, substrate lands, package housing, contact, solder and PCB, was developed for the Intel Dual Core E2180 processor. This developed model was shown to accurately simulate thermal behavior of the processor. Results from the thermal model of the processor provided data on the overall temperature distribution for several configurations that compared well to the experimental data obtained in Chapter 3.

Chapter 5

ELECTROTHERMAL ANALYSIS

In this chapter a method to design a new electrothermal analyzer is elaborated. This approach is based on coupling a circuit simulator and IR thermography measurements through an application program interface using the FLIR Software Development Kit (SDK) that updates the temperature information in near-real time. To examine the performance of the proposed electrothermal analyzer, DC analysis is performed on a power MOSFET circuit and the results of circuit parameters with and without temperature updating were obtained and discussed.

5. Electrothermal Analysis

The performance and characteristics of semiconductor components in electronic circuits can be considerably affected by temperature variations. Therefore, accurate electrothermal analysis method requires that the dynamic temperature effects induced by the heat dissipated in the circuit be taken into consideration.

Modeling electrothermal interactions in integrated circuits has been addressed in a variety of ways [56]. Based on the literature and available reports, existing methods can be broadly classified into two major methods: *direct* method and *relaxation*. In the direct method, the thermal model resembles an electrical circuit and the thermal and electrical problems are then solved simultaneously, while in the relaxation method the electrical and thermal systems are

solved separately and the solutions were obtained by applying successive relaxation between the two systems. Both methods are typically based on numerical and simulation results.

There are different numerical methods to solve the thermal problem (heat transfer equations) such as, Fourier series, finite difference method (FDM), finite element method (FEM), boundary element method (BEM), and extraction approximation approaches which are based on mathematical manipulation. An excellent review of these methods is reported in [6]. These numerical solution methods provide an *approximation* of the thermal behavior of the DUT. These methods always come with *assumptions and approximations* related to geometrical and material properties, discretisation of the heat transfer equations, coupling of multiple heat sources, etc.

In this research, a new electrothermal analyzer is proposed. The major difference between the proposed electrothermal analyzer and reported works in literature is in its thermal analysis method. The temperature distribution of the DUT is directly measured by IR thermography and is not based on simulation or calculation. Therefore, by using the experimental results the error percentage due to prediction of temperature by numerical methods is reduced significantly.

In our approach the temperature profile obtained from IR thermography measurement is coupled with the proper electrical model to update the temperature related parameters of DUT in near-real time condition.

5.1 Electrical Analysis

To perform electrical analysis on an integrated circuit, an electrical circuit simulator is needed. Every circuit simulator has a library which includes model definitions for each element type. In these models a set of equations are defined to specify the characteristics of the element.

One of the primary circuit simulators is called SPICE (Simulation Program with Integrated Circuits Emphasis) which was originally developed at the electronic research laboratory of the University of California, Berkeley in 1975. There are different versions of SPICE such as PSPICE which is a PC version of SPICE, and HSPICE which runs on UNIX workstations and large computers. In this research we used PSPICE as the electrical simulator [47].

5.1.1 MOSFET Pspice MODEL

The DUT in this study is a FDD8780 Fairchild Power MOSFET, [48]. To perform the electrothermal analysis of the MOSFET, the SPICE model parameters such as mobility, threshold voltage, saturation velocity, parasitic series resistance, and source/drain junction characteristics were modified to include temperature-dependent behavior. The inclusion of these parameters is described in the following sections.

a) Temperature dependence of mobility

Much research has been done to model the inversion charge mobility as a function of channel doping concentration, the gate and substrate voltages, and temperature. It is well known that phonon scattering, surface scattering, and columbic scattering (including ionized impurity scattering and interface charge scattering) are the three major scattering mechanisms governing the characteristics of carrier mobility in the inversion layer. For temperatures above 250K, phonon scattering is the dominant mechanism [49].

Several empirical unified formulas have been suggested to describe the mobility as a function of process parameters and bias conditions. However, all of them contain a quantity, E_{eff} that is not readily available for circuit simulation. It has been shown that E_{eff} may be expressed simply as $(V_{gs} + V_{th}) / (6T_{ox})$ [49]. In BSIM3 V3, a second order polynomial with parameters U_a , U_b , and U_c which are linear functions of temperature, is used to describe the temperature dependence of mobility [50].

For the MOSFET BSIM3 model, the mobility model including temperature effects becomes

$$\mu_{eff} = \frac{\mu_0 \left(\frac{T}{T_{NOM}} \right)^{U_{TE}}}{1 + (U_a(T) + U_c(T)V_{bseff}) \left(\frac{V_{gsteff} + 2V_{th}}{T_{OX}} \right) + U_b(T) \left(\frac{V_{gsteff} + 2V_{th}}{T_{OX}} \right)^2} \quad (5.1)$$

where

$$U_a(T) = U_A + U_{A1} \left(\frac{T}{T_{NOM}} - 1 \right) \quad (5.2)$$

$$U_b(T) = U_B + U_{B1} \left(\frac{T}{T_{NOM} - 1} \right) \quad (5.3)$$

$$U_c(T) = U_C + U_{C1} \left(\frac{T}{T_{NOM} - 1} \right) \quad (5.4)$$

where parameters μ_0 , U_A , U_{A1} , U_B , U_{B1} , U_C , U_{C1} , and U_{TE} can be extracted from the measured I-V data and T is the temperature in Kelvin. T_{nom} is the nominal temperature where the model parameters μ_0 , U_A , U_B , and U_C are extracted.

b) Temperature dependence of the threshold voltage

Threshold voltage (V_{th}) is another important parameter that is sensitive to temperature. It increases as temperature decreases due to the Fermi-level and band gap energy shifts. V_{th} depends linearly on the temperature over a wide range of temperature for devices with long channel lengths [49]. Recent experiments show that V_{th} rolloff, i.e. the dependence of V_{th} on V_{ds} and L (length of channel), is intensive to temperature. This can be explained by the fact that V_{th} rolloff results from the capacitive coupling of the drain and the channel, a temperature independent phenomenon.

The following temperature model of V_{th} is used in BSIM3 [50]:

$$V_{th}(T) = V_{th}(T_{NOM}, L, V_{ds}) + \left(K_{T1} + \frac{K_{T1L}}{L} + K_{T2} V_{bs} \right) \left(\frac{T}{T_{NOM}} - 1 \right) \quad (5.5)$$

where $V_{th}(T_{NOM}, L, V_{ds})$ is the threshold voltage value at T_{NOM} . The parameters K_{T1} , K_{T1L} , and K_{T2} are extracted from the experimental data and $\frac{K_{T1L}}{L}$ is a minor term introduced to improve the fitting accuracy.

The behavior of the threshold voltage (V_{th}) versus temperature for n-channel MOSFET with $W/L=6\mu m/0.25\mu m$ are given in Fig. 6.1. This shows that the temperature dependence of short channel effects can be well described by Eq. (5.5).

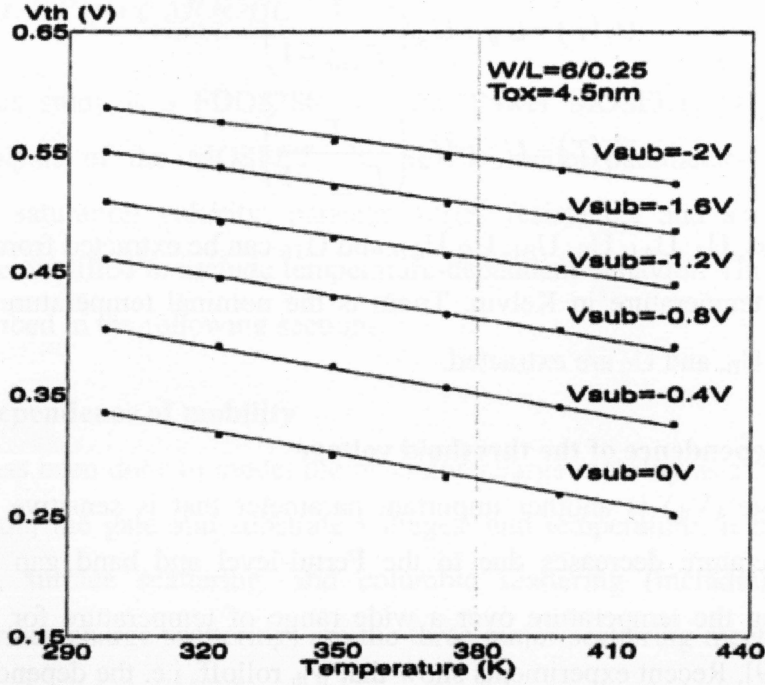


Figure 5.1: V_{th} -T data of a $W/L=6\mu m/0.25\mu m$ n-channel MOSFET at different V_{bs} [49].

c) Temperature dependence of the saturation velocity

It is known that the saturation velocity (V_{sat}) is a weak function of temperature. For simplicity, the temperature dependence of V_{sat} is usually ignored in the compact modeling of MOSFETs.

In BSIM3v3, the temperature dependence of V_{sat} is modeled with the following [50]:

$$v_{sat} = v_{sat,tnom} - A_T \left(\frac{T}{T_{NOM}} - 1 \right) \quad (5.6)$$

where A_T is a parameter extracted from the measured data, and v_{sat} is the saturation velocity at T_{NOM} .

d) Temperature dependence of the parasitic drain/source resistances

With the increasing current drive of MOSFETs and dropping supply voltages, the drain/source series resistance (R_{ds}) becomes a more important parameter. R_{ds} is composed of contact resistance, drain and source diffusion sheet resistance, and spreading resistance at the edge of the inversion layer due to current crowding. R_{ds} increases almost linearly with rising temperature.

In BSIM3 v3, R_{ds} and its temperature dependence is modeled as [50]:

$$R_{ds}(T) = \frac{R_{dsw}(T) \left[1 + P_{RWG} V_{gseff} + P_{RWB} \left(\sqrt{\phi_S - V_{bseff}} - \sqrt{\phi_s} \right) \right]}{W_{eff}^{WR}} \quad (5.7)$$

$$R_{dsw}(T) = R_{DSW,Tnom} + P_{RT} \left(\frac{T}{T_{NOM}} - 1 \right) \quad (5.8)$$

where R_{DSW} , P_{RWB} , P_{RWB} and W_R are extracted from the measured R_{ds} data at T_{NOM} . P_{RT} is extracted from the measured data at different temperatures. W_{eff} is the effective channel width without consideration of bias dependence. V_{gseff} is equal to $V_{gs} - V_{th}$ in the strong inversion region [50].

e) Temperature dependence of the S/D diode characteristics

For the source/drain junction in a MOSFET, the temperature dependences of the saturation current, I_s , and the junction capacitance at zero bias, C_{j0} , are important and need to be considered in the device model. The saturation current of a p-n junction is determined by the intrinsic carrier density, n_i , or the energy band gap of the material, E_g [49], both of which are temperature dependent. Similarly the Zero-bias junction capacitance is determined by the temperature dependent parameters dielectric constant of silicon material, ϵ_{si} , and the junction built-in potential, V_{bi} [49].

In BSIM3 v3, the temperature dependence of the Source to Bulk and Drain to Bulk junction is described by the saturation current I_{sbs} , the zero-bias unit area/perimeter junction capacitances $C_J(T)$, $C_{jsw}(T)$, and junction built-in potentials $P_b(T)$, $P_{bsw}(T)$ and $P_{bswg}(T)$.

I_{sb} is calculated as

$$I_{sbs} = J_s A_S + J_{ssw} P_S \quad (5.9)$$

$$I_{sbd} = J_s A_D + J_{ssw} P_D \quad (5.10)$$

where J_s is the saturation current density of the source or drain junction and A_S and A_D are the areas of the source and drain junctions. J_{ssw} is the saturation current density of the source or drain sidewall junction and P_S and P_D are the perimeters of the source and drain junctions. Both

J_S and J_{SW} are functions of temperature and are described by [50]. Figure 6.2 shows the current characteristics of the drain/bulk junction at several temperatures for the BSIM3 v3 diode model.

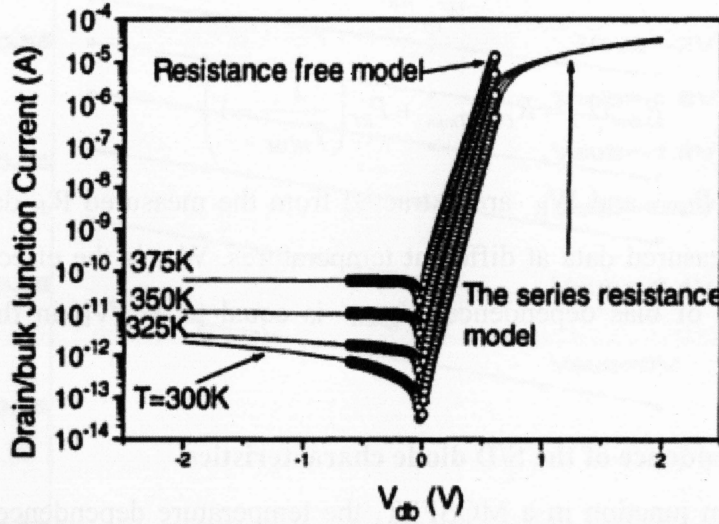


Figure 5.2: I-V characteristics of the drain/bulk junction at different temperatures [49].

The temperature dependence of the zero-bias junction capacitance is modeled with the following equations [49]:

$$C_j(T) = C_j [1 + T_{Cj} (T - T_{NOM})] \quad (5.11)$$

$$C_{jsw}(T) = C_{jsw} [1 + T_{Cjsw} (T - T_{NOM})] \quad (5.12)$$

$$C_{jswg}(T) = C_{jswg} [1 + T_{Cjswg} (T - T_{NOM})] \quad (5.13)$$

where $C_j(T)$, $C_{jsw}(T)$ and $C_{jswg}(T)$ are zero-bias junction capacitance per unit area, the perimeter junction capacitance per unit length at the field-oxide edge, and perimeter junction capacitance per unit length at the gate edge. C_j , C_{jsw} and C_{jswg} are the zero-bias capacitance at the nominal temperature T_{NOM} . T_{Cj} , T_{Cjsw} and T_{Cjswg} are the model parameters for the temperature coefficient of C_j , C_{jsw} and C_{jswg} .

The temperature dependence of the built-in potentials in the junction capacitances is modeled with the following equations [49]:

$$P_b(T) = P_b - T_{PB} (T - T_{NOM}) \quad (5.14)$$

$$P_{bsw}(T) = P_{BSW} - T_{PBSW}(T - T_{NOM}) \quad (5.15)$$

$$P_{bswg}(T) = P_{BSWG} - T_{PBSWG}(T - T_{NOM}) \quad (5.16)$$

where $P_b(T)$, $P_{bsw}(T)$, and $P_{bswg}(T)$ are the built-in potentials of the bottom junction, the periphery junction at the field -oxide edge, and the periphery junction at the gate edge at temperature T in Kelvin. P_B , P_{BSW} and P_{BSWG} are the built-in potentials of the bottom junction, the periphery junction at the field -oxide edge, and the periphery junction at the gate edge at temperature T_{NOM} . T_{PB} , T_{PBSW} and T_{PBSWG} are the temperature coefficients of the built-in potentials.

The $I_{ds}-V_{gs}$ characteristics for the n-channel MOSFET with $W/L=6\mu m/0.25\mu m$ at $V_{ds}=0.05V$ and $V_{bs}=0V$ is given in Fig. 5.3 for different temperature and the $I_{ds}-V_{ds}$ characteristics of the same MOSFET at $V_{gs}=2V$ and $V_{bs}=0V$ is given in Fig. 5.4 as well.

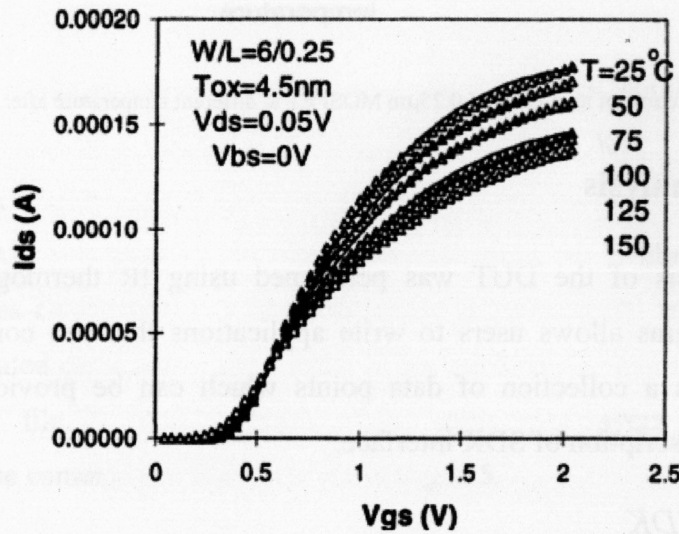


Figure 5.3: $I_{ds}-V_{gs}$ curve of an n-channel MOSFET of a $W/L=6\mu m/0.25\mu m$ at different temperature after Cheng et al. [49].

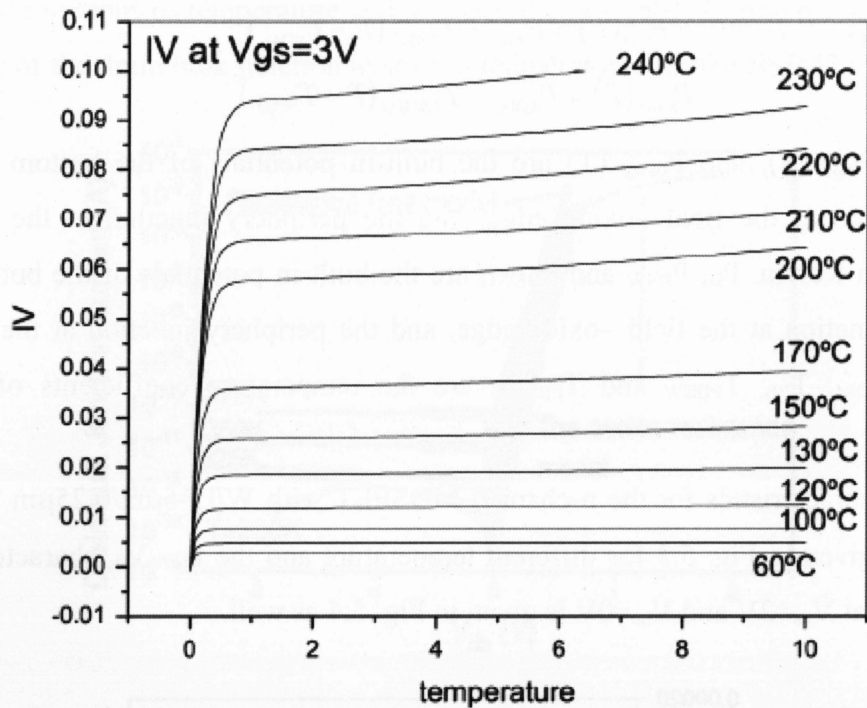


Figure 5.4: $I_{ds} - V_{ds}$ curve of an n-channel $0.25\mu\text{m}$ MOSFET at different temperature after Cheng et al. [49].

5.2 Thermal Analysis

The thermal analysis of the DUT was performed using IR thermography. The SDK of SC6000/SC4000 cameras allows users to write applications that can control and acquire the temperature profile as a collection of data points which can be provided to the simulator. Following is a brief description of SDK interface.

5.2.1 Camera SDK

Camera SC4000 SDK is a collection of several other SDKs, each with a specific function [51].

a) Accessories SDK

The Accessories SDK provides the interface for communicating with and acquiring image data from the camera. This SDK can discover available interfaces and devices, open a device,

read/write bytes to the control channel of the devices, and/or grab frames of image data from the device.

b) Phoenix Protocol (API)

The Phoenix Protocol API is responsible for formatting messages that use the phoenix protocol.

c) IACF Protocol (API)

The IACF Protocol API is responsible for formatting messages that use the IACF protocol.

d) Cielo SDK

The Cielo SDK provides functions for controlling the Cielo board in the SC6000/SC4000 camera. This board handles communications and some triggering tasks.

e) IACF SDK

The IACF SDK provides functions for controlling the SC6000/SC4000 camera core. Most of the functions called to control the SC6000/SC4000 are from this SDK.

f) IACF Util (API)

The IACF Util API contains utility functions for handling calibrated SC6000/SC4000 cameras. This includes changing the calibration range, converting camera data to temperature, saving/loading calibrated data files (.SEQ files). This API also contains a utility function for saving a 16-bit TIFF file. A brief overview of the component layers in an application that communicates with the camera core is diagramed in Fig. 5.5.

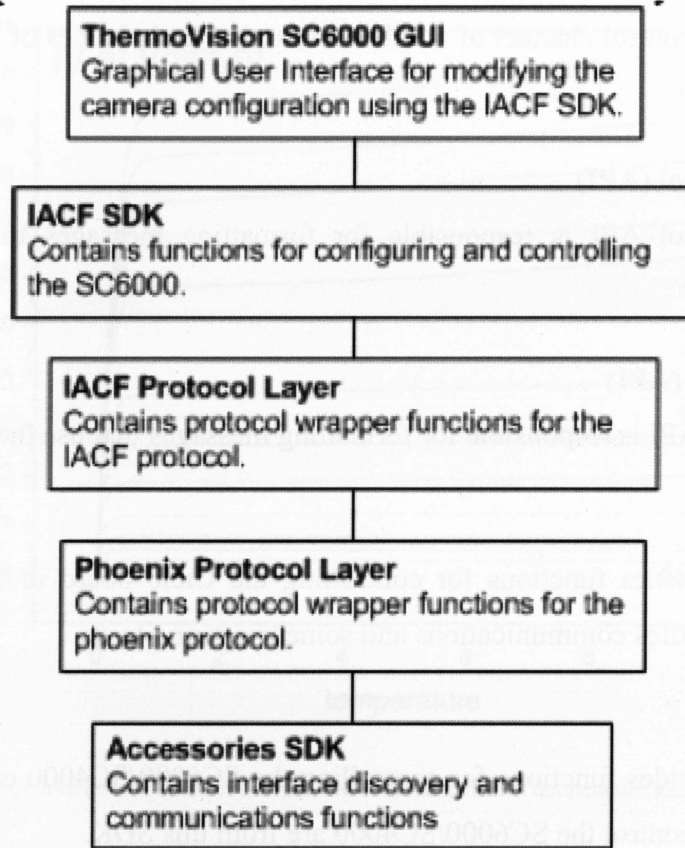


Figure 5.5: Camera SDK diagrams [52].

5.2.2 Temperature Profile by SDK

To obtain the temperature profile of the DUT a set of programs were written in Visual C++ 2008 by using the SDK functions as follow:

a) Set camera port :

A program was written to connect the camera over gigabyte Ethernet (GigE), USB or RS-232 interface. In this study the camera was connected by GigE due to its faster speed, allowing a higher frame rate.

b) Set camera IP:

The program must be configured to choose the correct IP address of the camera in order to perform calibration.

c) Set and save calibration

The output of camera is a set of raw data which should be calibrated before using. The SC4000 camera is calibrated for a range between -10°C to 360°C . "Set Calibration" is another program which is written to list all the calibration range in the camera and set the active one. After setting the active calibration, the camera output counts in the calibration range. The "Save Calibration" program is used to save the calibration data to disk.

d) Acquire data

This program acquires raw frames from the camera and saves them to disk. The window size(X, Y) and number of frames (N) should be specified in this section. There will be N Excel files generated, each contains X rows and Y columns of temperature data.

e) Apply calibration

The result of acquire data is a set of raw output which should be calibrated to show the actual temperature. The "Apply Calibration" is used to apply the saved calibration file to the acquired data.

f) Select the position of DUT and create thermal profile

The SDK output is a set of files with specified window size. To have the temperature profile of the DUT the position of the device should be clear. Another program was written to read the frames one by one and select the temperature data of a specified row and column corresponding to the position of DUT and save them in another file.

5.3 Methodology of IR Thermography and PSPICE Simulator Coupling

An electrothermal measurement-simulation method has been developed by coupling the IR thermography measurement and PSPICE simulator to update the temperature related parameters of DUT in near real time condition. Visual C++ was chosen as the environment to transfer the measured data to the simulator.

5.3.1 Implemented Algorithm

The flowchart of the developed algorithm is shown in Fig. 5.6. The procedure begins by running the SDK to obtain the temperature profile of the DUT. The setup steps mentioned in section 5.2.2 should be performed to obtain the temperature profile. The temperature is imported to PSPICE as an include file and SPICE is run for specified temperature. To avoid computing of very close temperatures in electrical model, a convergence parameters ϵ is considered as the temperature difference between 2 frames. The electrical simulation is performed if the difference is greater than the specified ϵ . The simulation is continued till last temperature which is related to the last frame.

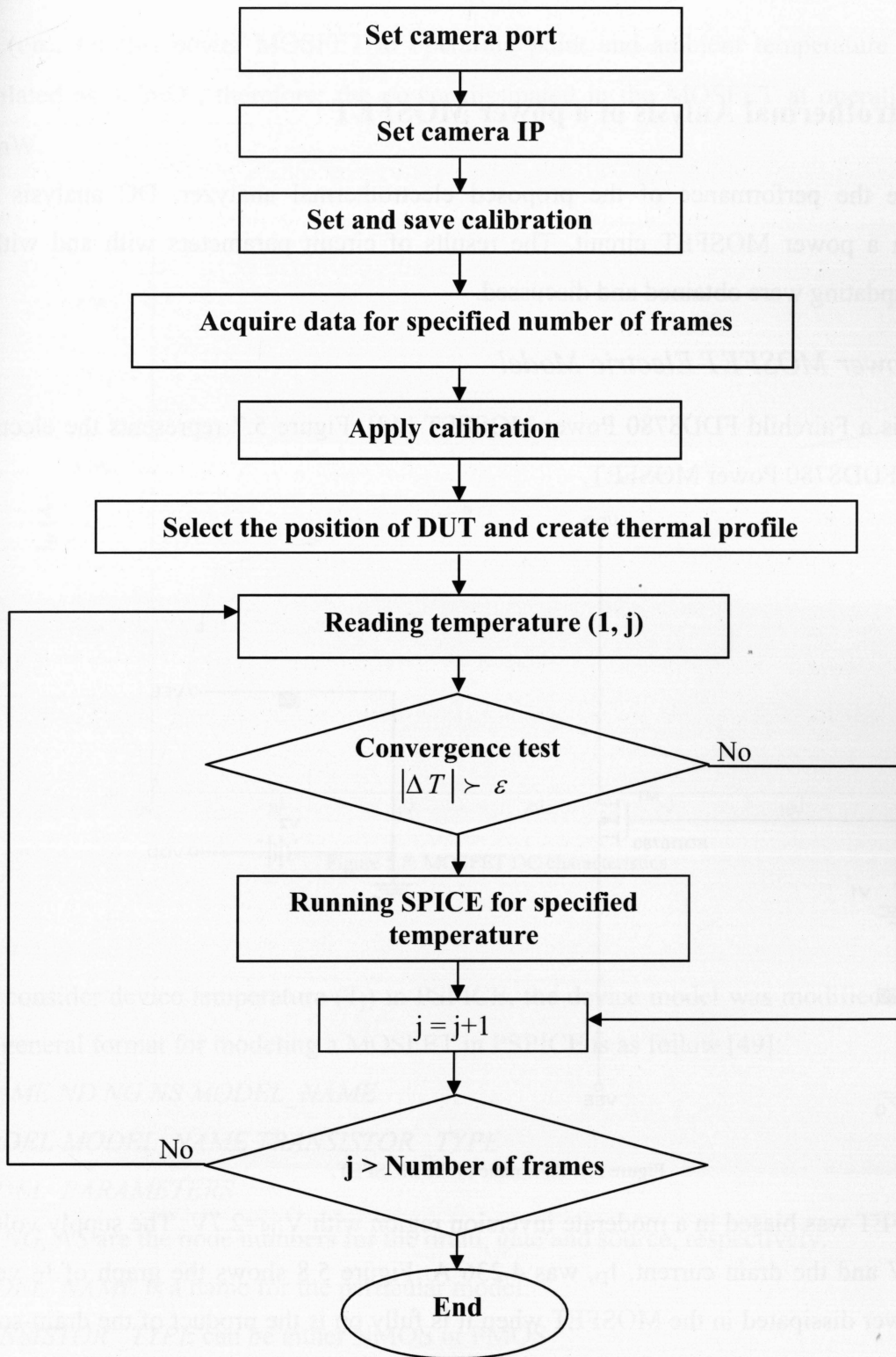


Figure 5.6: Flowchart of the electrothermal analysis.

5.4 Electrothermal Analysis of a power MOSFET

To examine the performance of the proposed electrothermal analyzer, DC analysis was performed on a power MOSFET circuit. The results of circuit parameters with and without temperature updating were obtained and discussed.

5.4.1 Power MOSFET Electric Model

The DUT is a Fairchild FDD8780 Power MOSFET [48]. Figure 5.7 represents the electrical circuit of the FDD8780 Power MOSFET.

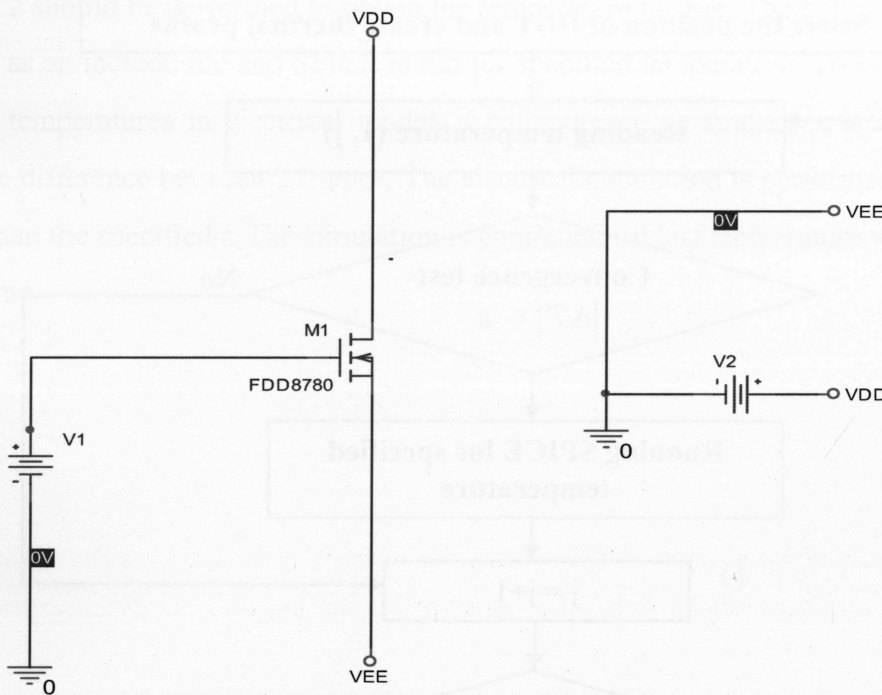


Figure 5.7: Schematic of the MOSFET.

The MOSFET was biased in a moderate inversion region with $V_{GS}=2.7V$. The supply voltage, V_{DD} was 10V and the drain current, I_D , was 4.236 A. Figure 5.8 shows the graph of I_D versus V_{DD} . The power dissipated in the MOSFET when it is fully on is the product of the drain-source voltage and the current flowing through the device. The voltage across the MOSFET in this case will be the drain-source resistance of the MOSFET, $R_{DS} (on)$ times the current. The resistance,

$R_{DS} (on)$, for this power MOSFET at operating point and ambient temperature of $25^{\circ}C$ was simulated as $3.7m\Omega$, therefore; the power dissipated in the MOSFET at operating point was 66 mW.

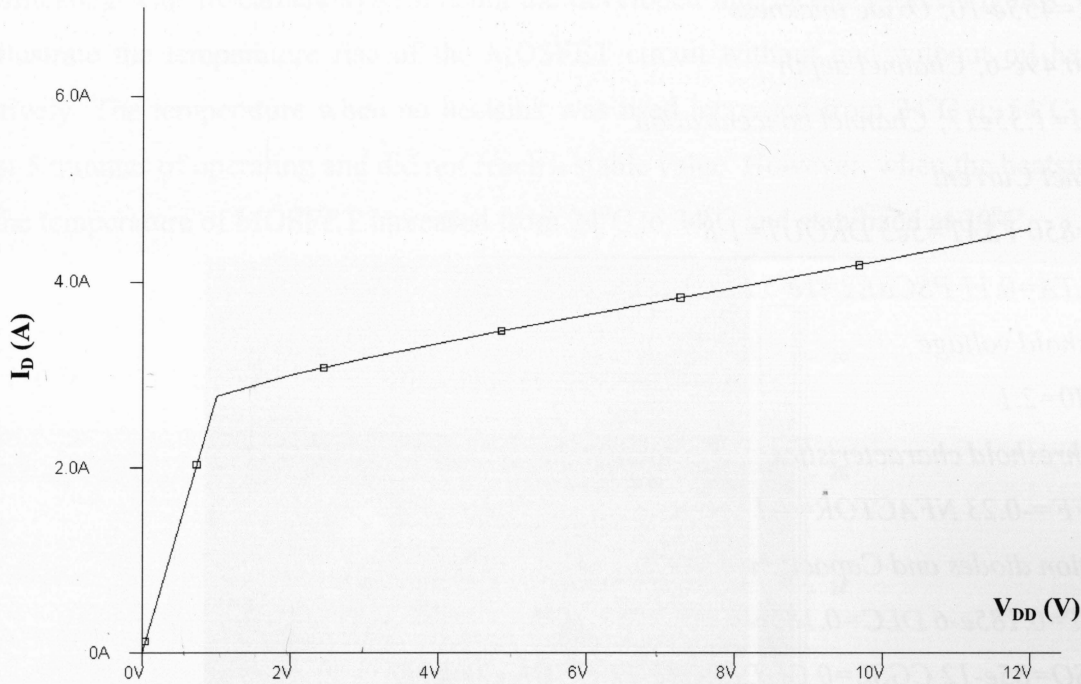


Figure 5.8: MOSFET DC characteristics.

To consider device temperature (T_j) in PSPICE, the device model was modified to include T_j . The general format for modeling a MOSFET in PSPICE is as follow [49]:

MNAME ND NG NS MODEL_NAME

.MODEL MODEL_NAME TRANSISTOR_TYPE

MODEL_PARAMETERS

ND, NG, NS are the node numbers for the drain, gate and source, respectively.

MODEL_NAME is a name for the particular model.

TRANSISTOR_TYPE can be either NMOS or PMOS

MODEL_PARAMETERS are the parameters that model the MOSFET characteristics. Device junction temperature is included in these parameters.

The SPICE model of FDD8780 was modified to include the temperature dependent parameters and junction temperature as follow:

.MODEL Bsim3 NMOS (LEVEL=7 VERSION=3.1 MOBMOD=3 CAPMOD=2 paramchk=1

**Process Parameters*

+ *TOX=455e-10; Oxide thickness*

+ *XJ=0.49e-6; Channel depth*

+ *NCH=1.35e17; Channel concentration*

**Channel Current*

+ *U0=850 VSAT=5e5 DROUT=1.8*

+ *DELTA=0.11 PSCBE2=1e-5 RSH=1.63e-3*

**Threshold voltage*

+ *VTH0=2.1*

**Sub-threshold characteristics*

+ *VOFF=-0.23 NFACTOR=1.1*

**Junction diodes and Capacitance*

+ *LINT=0.185e-6 DLC=0.185e-6*

+ *CGSO=85e-12 CGSL=0 CGDO=38e-12 CGDL=270e-12*

+ *CJ=0 CF=0 CKAPPA=1.8*

** Temperature parameters*

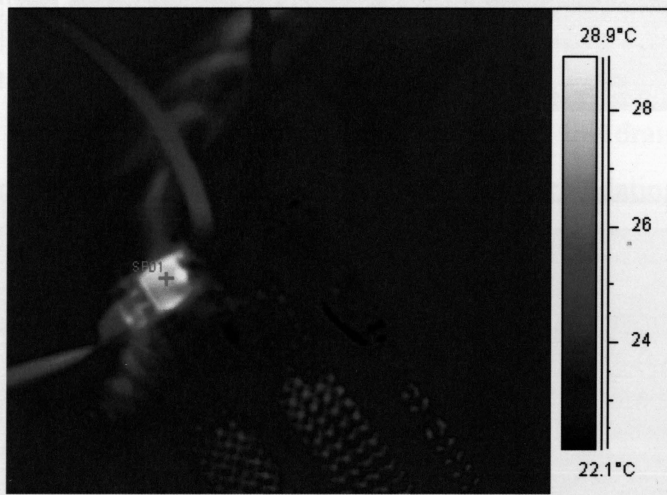
+ *KT1=-1.1 KT2=0.022 UA1=0.6e-8 UB1=-7.61e-18 UC1=0.056*

+ *UTE=-1.5 XTI=3.0 NJ=10*

+ *T_ABS=<Tj>)*

5.4.2 Power MOSFET IR Thermography

The circuit shown in Fig. 5.9 was biased at an operating point, $V_{GS}=2.7V$, $V_{DD}=10V$, and the thermal profile of the MOSFET with and without an oil heatsink was obtained by communicating with IR camera system using the developed interface program. Figures 5.9 and 5.10 illustrate the temperature rise of the MOSFET circuit without and without oil heatsink, respectively. The temperature when no heatsink was used increased from $24^{\circ}C$ to $54^{\circ}C$ during the first 5 minutes of operating and did not reach a stable value. However, when the heatsink was used, the temperature of MOSFET increased from $24^{\circ}C$ to $34^{\circ}C$ and stabilized at $30^{\circ}C$.



(a)

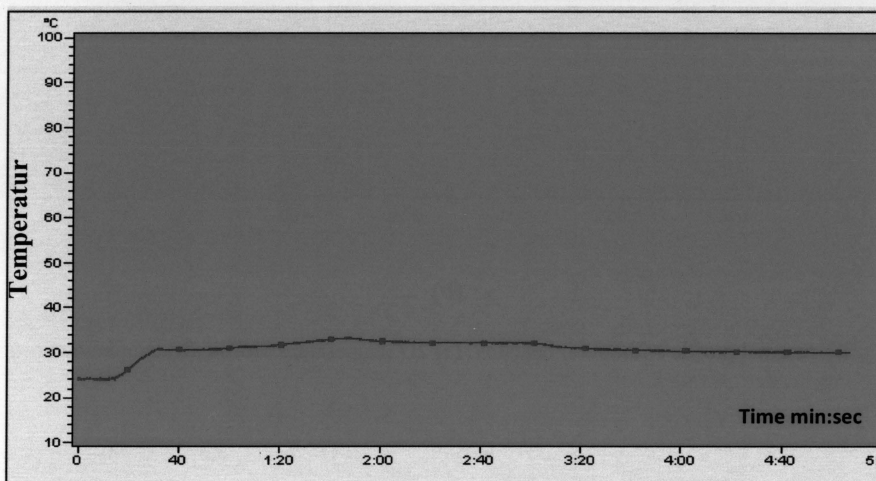
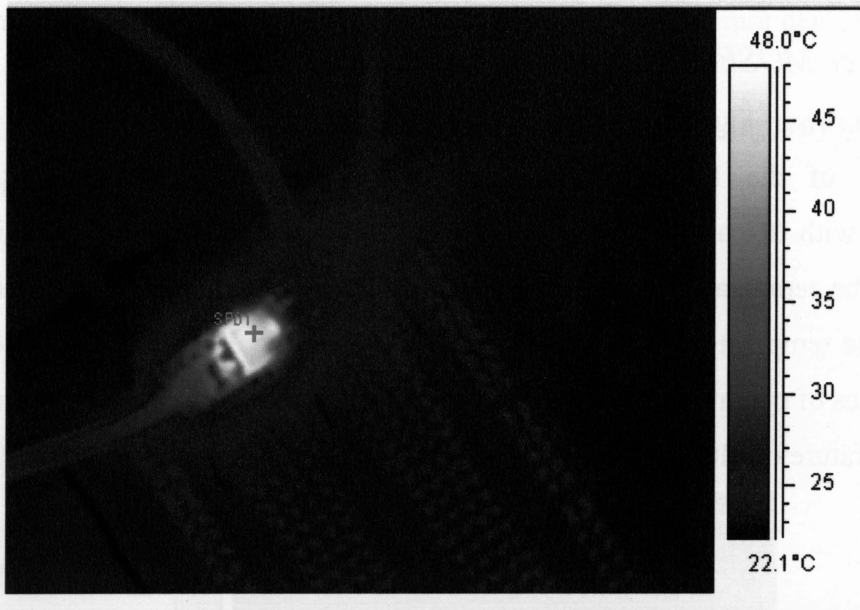
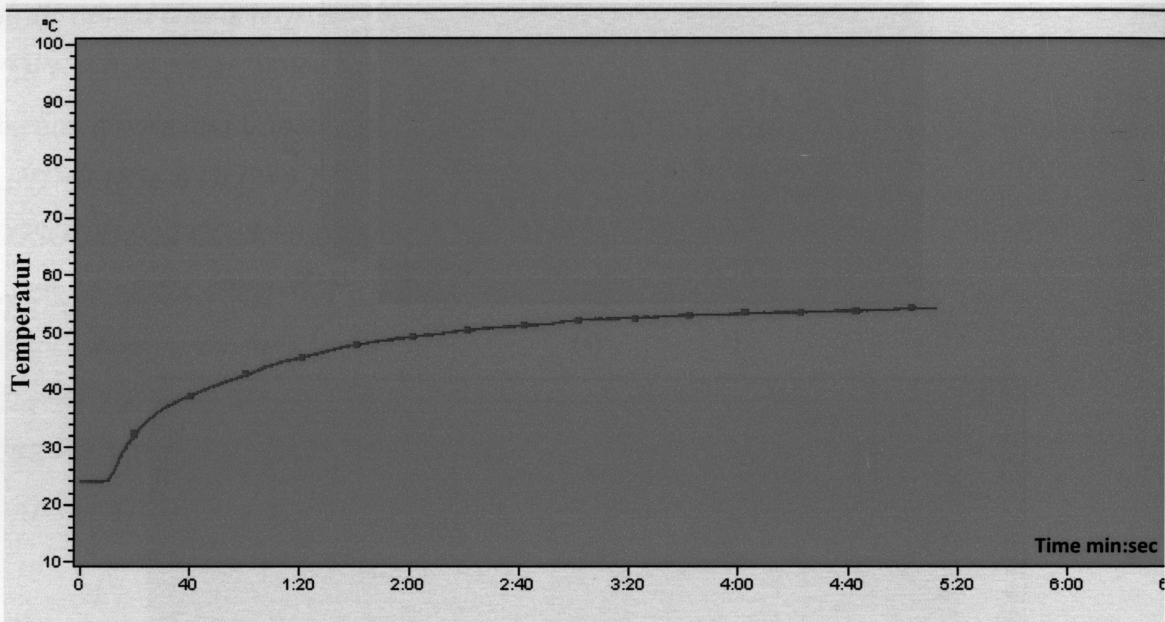


Figure 5.9: MOSFET thermal profile with oil heatsink, (a) 2D temperature profile, (b) temperature profile versus time .



(a)



(b)

Figure 5.10: MOSFET thermal profile without oil heatsink, (a) 2D temperature profile, (b) temperature profile versus time.

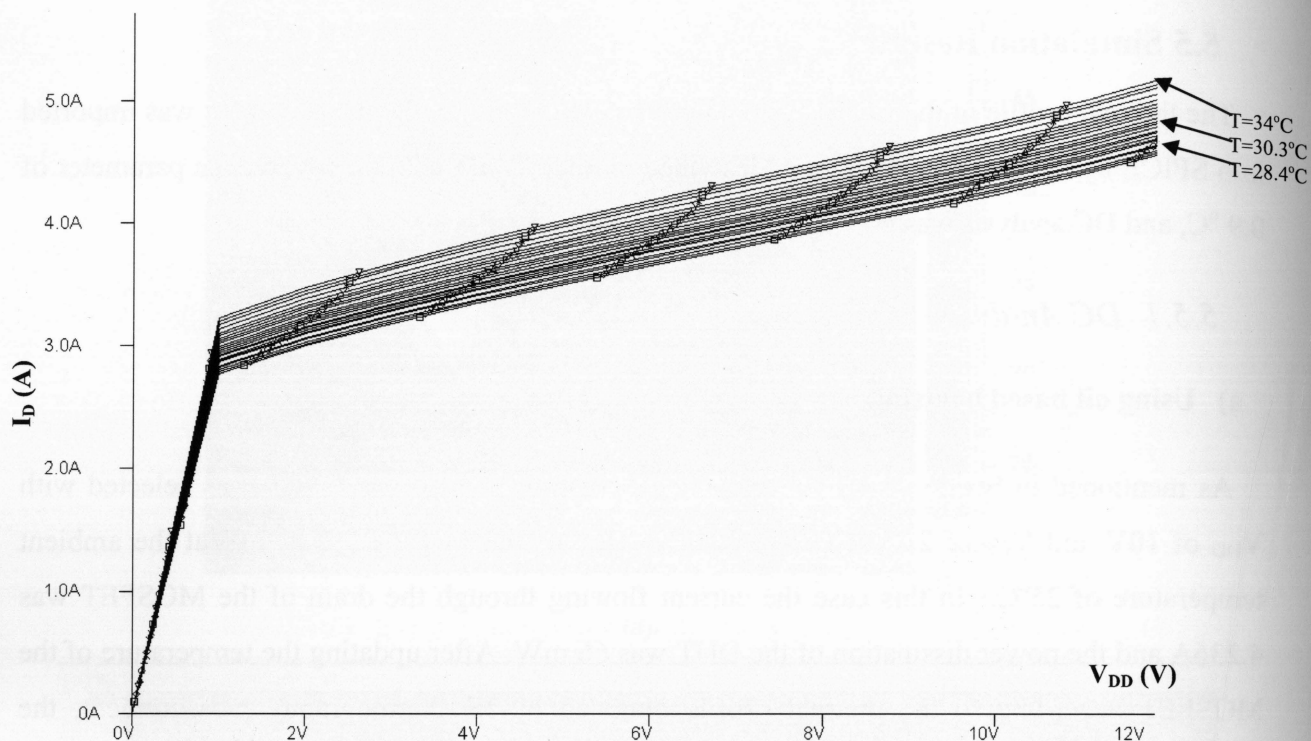
5.5 Simulation Results

The thermal profile of the MOSFET obtained by IR thermography measurement was imported into SPICE by using the methodology described in Section 5.3 with a convergence parameter of 0.9°C , and DC analysis was performed on the circuit.

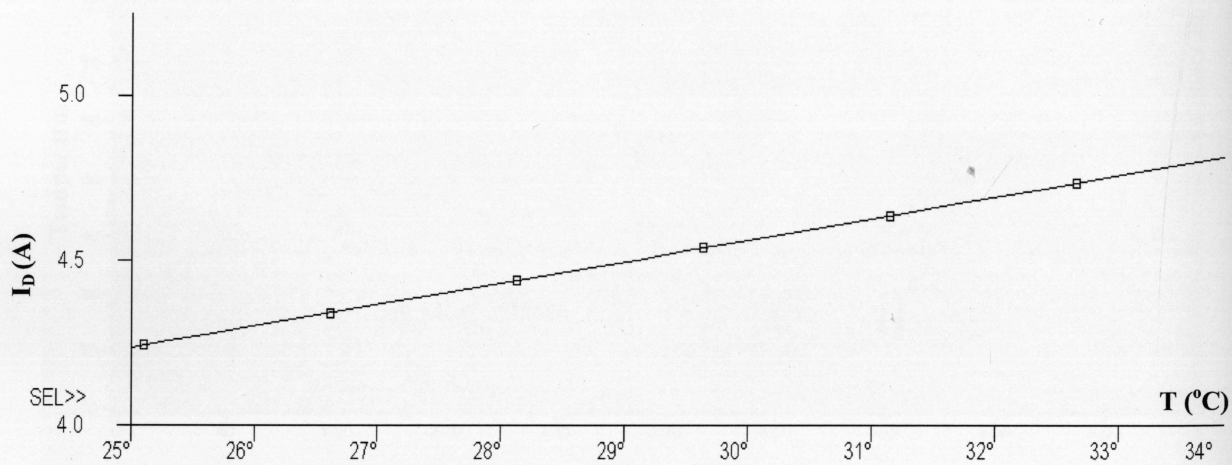
5.5.1 DC Analysis

a) Using oil based heatsink

As mentioned in Section 5.4.1 the moderate operating point of MOSFET was selected with V_{DD} of 10V and V_{GS} of 2.7V. The threshold voltage of the MOSFET was 2.0V at the ambient temperature of 25°C . In this case the current flowing through the drain of the MOSFET was 4.236A and the power dissipation of the DUT was 66 mW. After updating the temperature of the MOSFET according to the thermal profile obtained by IR thermography measurement, the MOSFET current changed as shown in Fig. 5.11 (a) and (b).



(a)

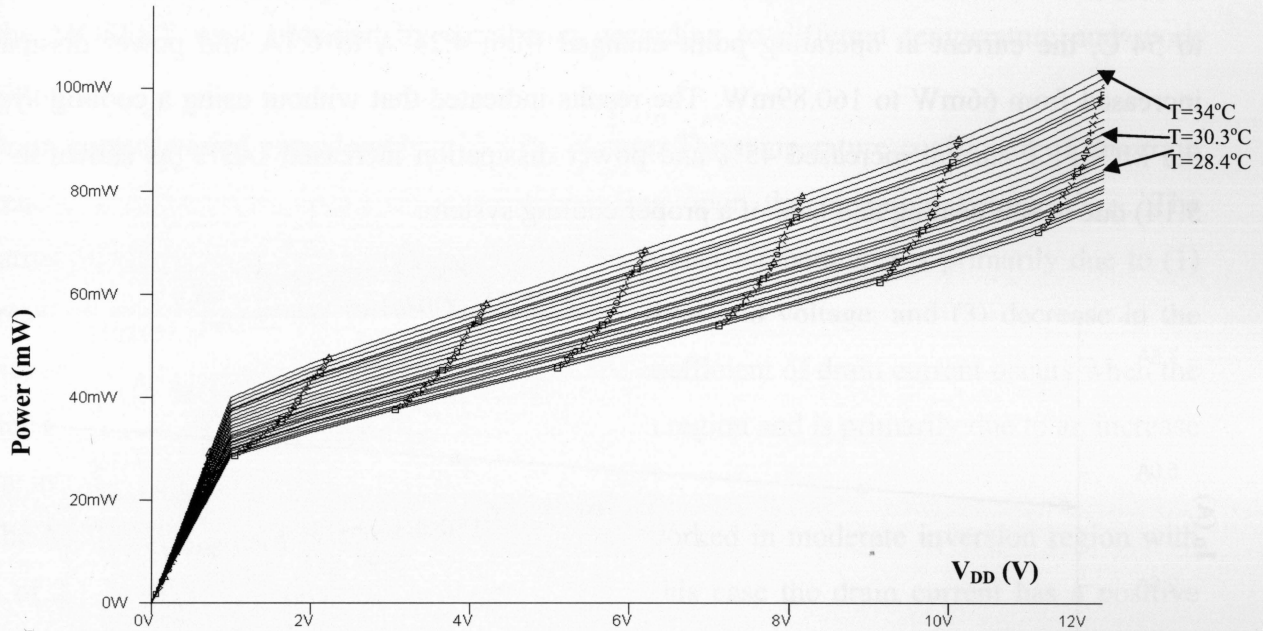


(b)

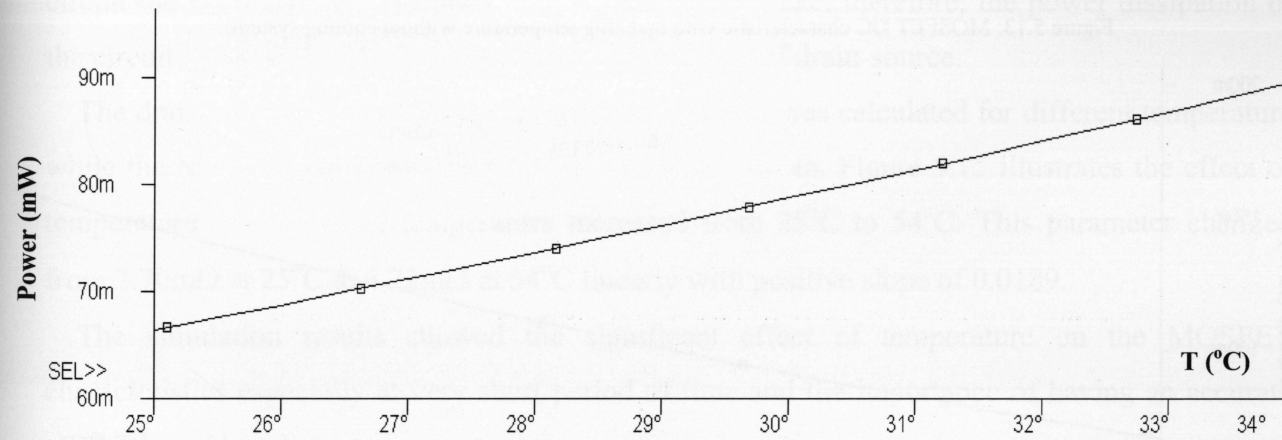
Figure 5.11: MOSFET DC characteristic with updating temperature with cooling system (a) I_d versus V_{DD} , (b) I_d versus temperature.

As Fig. 5.11 (b) shows, the current of the MOSFET at operating point increased from 4.236 A to 4.823A and consequently the power dissipation changed from 66mW to 89.74mW which

means 13% increase in current and 35% increase in power dissipation. Figures 5.12 (a) and (b) illustrate the power dissipation of the MOSFET with temperature increase.



(a)



(b)

Figure 5.12: MOSFET power dissipation with updating temperature with cooling system, (a) Power versus V_{DD} , (b) Power versus temperature.

b) Without using heatsink

The thermal profile of the MOSFET while working without cooling system was imported into SPICE and the results of DC analysis are shown in Fig 5.13. As temperature increased from 25°C to 54°C, the current at operating point changed from 4.24 A to 6.1A and power dissipation increased from 66mW to 160.89mW. The results indicated that without using a cooling system the MOSFET current increased 45% and power dissipation increased 143% (as shown in Fig. 5.14) due to self heating and lack of a proper cooling system.

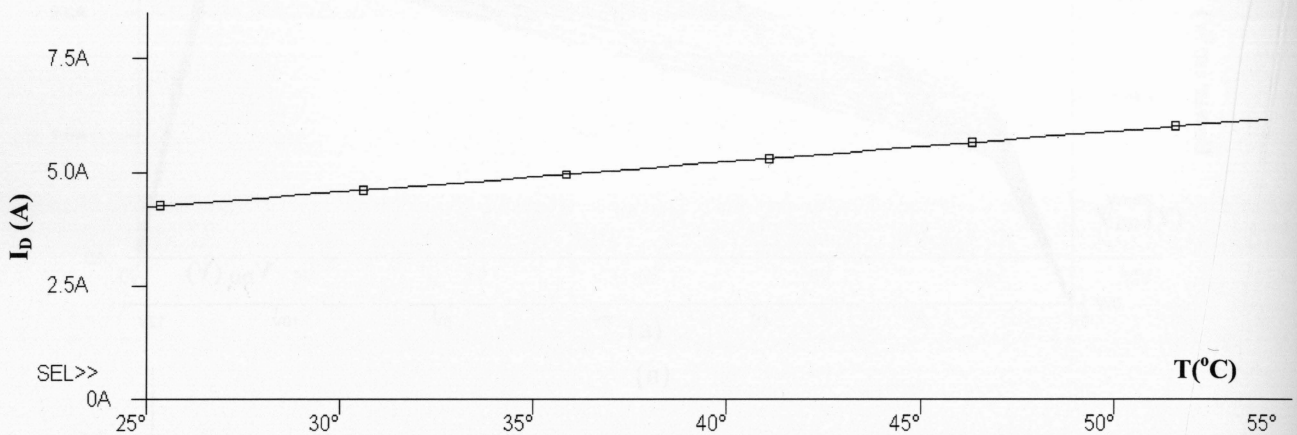


Figure 5.13: MOSFET DC characteristic with updating temperature without cooling system.

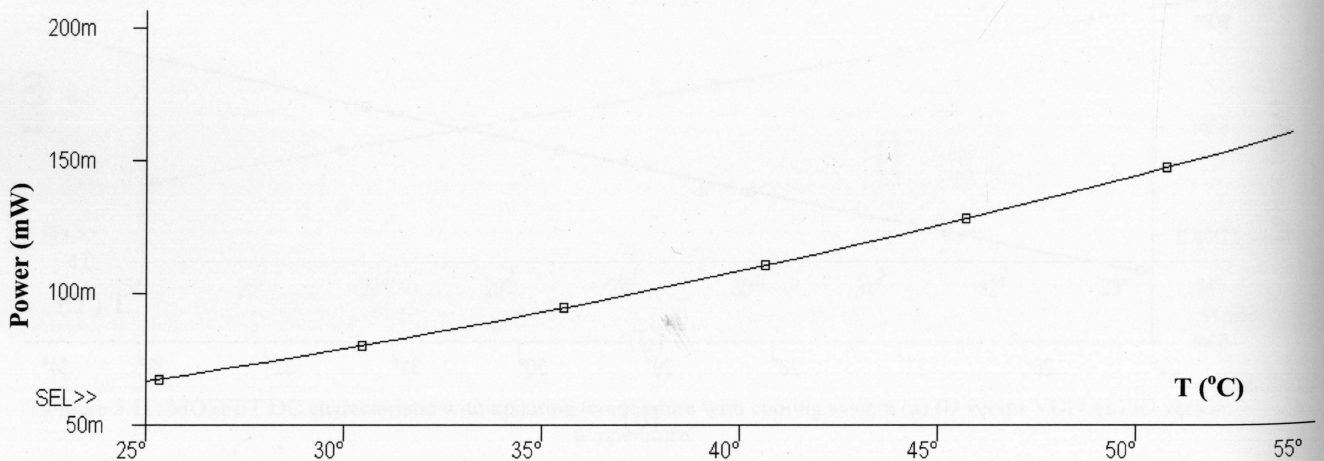


Figure 5.14: MOSFET power dissipation with updating temperature without cooling system.

5.6 Discussion

As mentioned in Section 5.1.1, the MOSFET characteristics are strongly temperature dependent. Here two important characteristics including I-V characteristic and power dissipation of the MOSFET were obtained by simulation according to different temperature and work conditions.

Drain current varied considerably with temperature. The temperature coefficient of the drain current can be positive, negative or zero depending upon the operating voltage, V_{GS} . The negative temperature coefficient of drain current (at higher temperature) is primarily due to (1) decrease in the carrier mobility, (2) increase in the threshold voltage, and (3) decrease in the carrier saturation velocity. The positive temperature coefficient of drain current occurs when the device is operating in the weak and moderate inversion region and is primarily due to an increase in the intrinsic carrier concentration [54].

The MOSFET circuit tested in previous sections, worked in moderate inversion region with V_{GS} of 2.7 V while the threshold voltage is 2V. In this case the drain current has a positive temperature coefficient and the simulation results showed this fact.

Another parameter which changed by temperature significantly was power dissipation. In our circuit the MOSFET was working fully on and in one state, therefore; the power dissipation of the circuit was mostly resistive power due to resistance of drain-source.

The drain-source resistance ($R_{DS(on)}$) of the MOSFET was calculated for different temperature while the MOSFET was working without a cooling system. Figure 5.15 illustrates the effect of temperature on R_{DS} while temperature increased from 25°C to 54°C. This parameter changed from 3.70m Ω at 25°C to 4.22m Ω at 54°C linearly with positive slope of 0.0189.

The simulation results showed the significant effect of temperature on the MOSFET characteristics especially at very short period of time and the importance of having an accurate electrothermal analyzer.

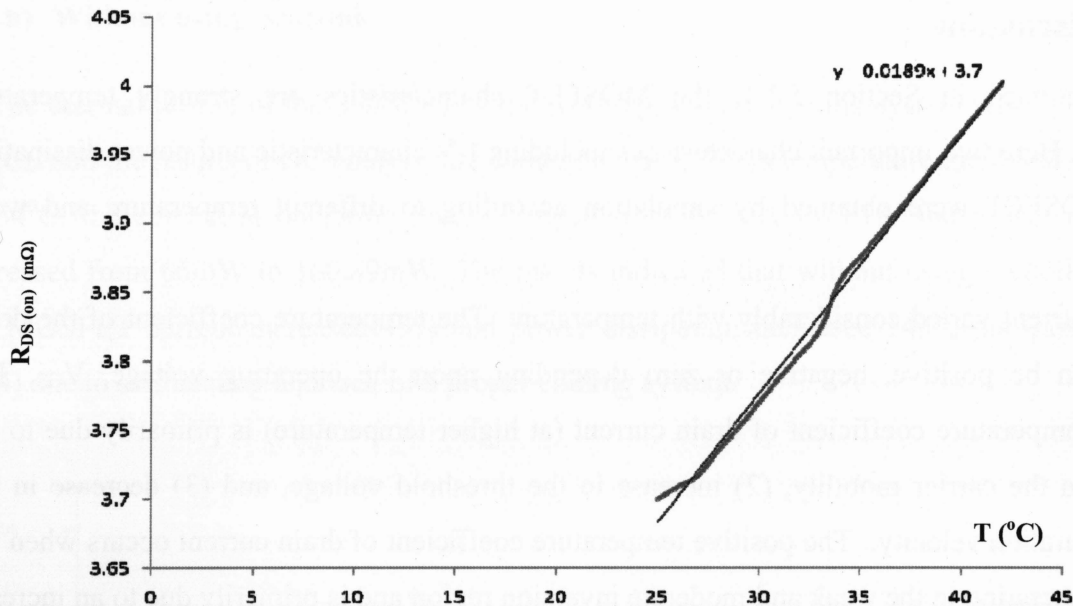


Figure 5.15: $R_{DS(on)}$ of MOSFET during DC analysis without oil cooling system versus temperature.

5.7 Summary

A new electrothermal analysis method to investigate the effect of temperature on semiconductor components characteristics was introduced. The coupling procedure of the electrical simulator and IR thermography measurement through software development kit and Visual C++ were discussed in detail.

The proposed electrothermal analyzer was employed to investigate the thermal effect in a power MOSFET circuit with and without using oil based heatsink. The DC analysis was performed on the circuit. The obtained results indicated that by using a cooling system, the temperature increase of 9°C, changed the current and power dissipation of the system approximately 13% and 35% respectively and consequently changed the operating point of the system. In addition, the system was operated without a cooling system which showed 45% increase in current and 143% increase in power dissipation due to 30°C temperature difference.

Chapter 6

6. Conclusions and Future Work

In this thesis a methodology, implementation and validation of an experimental infrared measurement technique for the thermal and electrothermal analysis of electronic circuits was presented. The electrothermal analysis was based on coupling a circuit simulator and IR thermography measurement through an application program interface that updates the temperature information in near-real time. The experimental setup is capable of performing steady state and transient analyses.

The proposed setup was used to perform the thermal analysis and power measurement of an Intel Dual Core E2180 processor. The power dissipation of the processor was obtained by calculating and measuring the heat transfer coefficient of the oil heatsink while the processor was executing SPEC CPU 2006 standard benchmark. Moreover, the power consumption of the processor was measured. The obtained results by IR thermography showed that around 80% of the total power consumption in processor is dissipated as heat.

Validation of experimental results was performed by development of a finite element thermal model for the processor. The developed model was shown to accurately simulate thermal behavior of the processor. Results from the thermal model of the processor provided data on the overall temperature distribution for several configurations that compared well to obtained experimental data. In addition, the model was simulated for the data sheet thermal profile of the processor and the maximum error percentage of 2.77% was obtained.

The DC electrothermal analysis of a Fairchild Power MOSFET was performed to examine the performance of the designed electrothermal analyzer. The MOSFET was biased in a moderate inversion region. The supply voltage, V_{DD} was 10V and the drain current, I_D , was 4.236 A. The thermal profile of the MOSFET was obtained by using oil heatsink and without it. The thermal profile was imported into SPICE model of the MOSFET. The temperature without heatsink

increased from 24°C to 54°C during the first 5 minutes of running and did not reach a stable point. However by using a heatsink the temperature of MOSFET increased from 24°C to 34°C and stabilized at 30°C.

Two important parameters including I-V characteristics and power dissipation of the MOSFET were obtained according to different temperature and work condition. The obtained results showed that the drain current increased considerably with temperature due to its positive temperature coefficient in moderate inversion mode. With an oil heatsink the drain current of the MOSFET at operating point increased from 4.236A to 4.823A and consequently the power dissipation changed from 66mW to 89.74mW- a 13% increase in current and 35% increase in power dissipation. Also the results of analysis without using heatsink indicated that as temperature increased from 25°C to 54°C, the drain current changed from 4.24 A to 6.1A and power dissipation increased from 66mW to 160.89mW. The results indicated that without using cooling system the MOSFET current increased 45% and power dissipation increased 143% due to self heating and poor cooling system.

In addition, the drain-source resistance ($R_{DS(on)}$) of the MOSFET was obtained for different temperature at operating point. It changed from 3.70mΩ at 25°C to 4.22mΩ at 54°C. The analysis results showed the significant effect of temperature on the MOSFET characteristics especially at very short period of time and the importance of having an accurate electrothermal analyzer.

The major difference between the proposed electrothermal analyzer and reported works in literature is in its thermal analysis method. The temperature distribution of the DUT is directly measured by IR thermography and is not based on simulation or calculation. Therefore, by using the experimental results the error percentage due to prediction of temperature by numerical methods is reduced significantly.

In general, by this work we would like to emphasize on the importance of performing electrothermal analysis on integrated circuits. It was shown that thermal issues are critical and must be considered during their early design phase. Although electrothermal analysis is more time consuming than electrical analysis, more accurate evaluation of the circuit performance can be obtained.

Hopefully in the future we would like to optimize the developed electrothermal analysis tool with crucial aspect being analysis of both spatial and temporal variations in the electrical and thermal system and their interaction. This will allow accurate assessment of performance of electronic products and systems to avoid high risk of overheating causing early device failure.

References

- [1] M. Pedram and S. Nazarian, "Thermal modeling, analysis, and management in VLSI circuits: Principles and methods," *Proceedings of the IEEE*, vol.94, no.8, pp.1487-1501, Aug. 2006.
- [2] F. A. Mohammadi, K. Meres, and M.C.E. Yagoub, "Thermal analysis of the interconnect metals in integrated circuits," *WSEAS Transactions on Circuits and Systems*, vol. 4, no. 2, pp. 155-160, Feb. 2005.
- [3] F. A. Mohammadi and S. Sharifian Attar, "Development of an electro-thermal simulation tool for integrated circuits," *Canadian Journal of Electrical and Computer Engineering (CJECE)*, vol. 33, Issue 3, 2008.
- [4] C. Isci and M. Martonosi, "Runtime power monitoring in high-end processors: Methodology and empirical data," *Proceedings of the 36th annual IEEE/ACM International Symposium on Microarchitecture*, pp.93-104 , 2003.
- [5] F. A. Mohammadi, K. Meres, and M. C. E. Yagoub, "Rigorous thermal treatment of heat generation and heat transfer in GaAs-based HBT device modeling," *Proceedings of EuroSIME2005*, pp. 604-608, April 2005, Germany.
- [6] S. Sharifian Attar, "Development of an electrothermal simulation tool for integrated circuits," Master Thesis, Ryerson University, Toronto, ON, Canada, Sept. 2007.
- [7] WEST MARINE Company, Oil pump data sheet, [Online document] 2008, Available at <http://www.westmarine.com>.
- [8] Flir ThermoVision®SC4000 thechnical specification data sheet, [Online document] ,2005 , Available at www.infraredresearchcameras.com.

- [9] J. Stasiek, A. Stasiek, and M. Jewartowski, "Liquid crystal thermography and true colour digital image processing," *Optic and Laser Thechnology*, vol. 38, no. 4-6, pp. 243-256, 2005.
- [10] M. Parsley, "The use of thermochromic liquid crystals in research applications , thermal mapping and non-destructive testing," *Semiconductor Thermal Measurement and Management IEEE Symposium*, vol. 12, pp.53-58 , 1991.
- [11] K. Azar and J. R. Benson, "Liquid crystal imaging for temperature measurement of electronic devices," *IEEE Measurement and Management Symposium*, pp. 23-33, 1991.
- [12] J. Christofferson, D. Vashae, A. Shakouri, and P. Melese, "High resolution non-contact thermal characterization of semiconductor devices," *Proceedings of the SPIE*, vol. 4275, pp.24-25 , 2001.
- [13] S. Grauby, B. C. Forget, S. Holé, and D. Fournier, "High resolution photothermal imaging of high frequency phenomena using a visible CCD camera associated with a multichannel lock-in scheme," *Review of Scientific Instrument Journal*, vol. 70, no. 9, pp. 3603–3608, 1999.
- [14] V. Quintard, G. Deboy, S. Dilhaire, D. Lewis, T. Phan, and W. Claeys, "Laser beam thermography of circuits in the particular case of passivated semiconductors," *Microelectron. Eng.*, vol. 31, pp. 291–298, 1996.
- [15] S. Grauby, S. Dilhaire, S. Jorez, and W. Claeys, "Temperature variation mapping of a microelectromechanical system by thermorefectance imaging," *IEEE Electron Device Letters*, vol. 26, Feb.2005.
- [16] J. Heller, J. W. Bartha, C. C. Poon, and A. C. Tam, "Temperature dependence of the reflectivity of silicon with surface oxide at wavelengths of 633 and 1047 nm," *Appl. Phys. Lett.*, vol. 75, no. 1, pp. 43–45, 1999.

- [17] K. Piers'cin' ski, D. Piers'cin' ska, and M. Bugajski, "Quantification of thermoreflectance temperature measurements in high-power semiconductor devices—lasers and laser bars," *Microelectronics Journal*, vol. 40, pp.1373-1378, 2009.
- [18] A. Majumdar, "Scanning thermal microscopy," *Annual Review of Materials Science*, vol. 29, pp. 505-585, 1999.
- [19] Ph. Dobson, J. M. R. Weaver, and G.Mills, "New methods for calibrated scanning thermal microscopy (SThM) ," *IEEE SENSORS Conference*, vol.31, pp. 708-711, 2007.
- [20] R. Audbry and P. Dobson, "SThM temperature mapping and nonlinear thermal resistance Evolution with bias on AlGaIn/GaN HEMT devices," *IEEE Transactions on Electron Devices*, vol. 54, pp. 385-390, 2007.
- [21] T. Leinhos. M. Stopka, and E. Oesterschulze, "Micromachined fabrication of Si cantilevers with schottky diodes integrated in the tip," *Applied Physics*, vol. A66, pp. S65-S69, 1998.
- [22] H. Zhou, G. Mills, B. K. Chong, A. Midha, L. Donaldson, and J. M. R. Weaver, "Recent progress in the functionalization of atomic force microscopy probes using electron-beam nanolithography," *Journal of Vacuum Science and Technology*, vol. 17, pp. 2233-2239, 1999.
- [23] M. H. Li, J. J. Wu, and Y. B. Gianchandani, "Surface micromachined polyimide scanning thermocouple probes," *Journal of Microelectromechanical Systems*, vol. 10, pp. 3-9, 2001.
- [24] K. Tanaka, H. Kuwano, and S. Nagasawa, "A novel scanning thermal microscopy system," *IEEE 20th Int. Conference On Micro Electro-Mechanical Systems*, pp. 627-630, Japan, 2007.
- [25] R. A. Epperly, G. E. Heberlein, and L. G. Eads, "Thermography, a tool for reliability and safety," *IEEE Industry Applications Magazine*, vol. 5, no. 1, pp. 28-36, 1991.

- [26] FLIR company, "Thermography history," [Online document], June 2009, Available at http://www.flirthermography.com/about/ir_history.asp.
- [27] FLIR company, "How does infrared camera work?," [Online document], June 2009, Availabe at http://www.flirthermography.com/about/how_infrared_cameras.asp.
- [28] FLIR company, "Why IR thermography?," [Online document], June 2009, Availabe at http://www.flirthermography.com/about/why_ir.asp.
- [29] E. Salem and D. Ibitayo, "Validation of infrared camera thermal measurements on high voltage power electronics components," *IEEE Transactions of Instrumentation and Measurement* , vol. 56, no. 5, October 2007.
- [30] M. Paniccia, "Method for cooling of a semiconductor device using an infrared transparent heatsink," *United states patent*, US 6251706 B1, June 2001.
- [31] J. Lacey , A. Weger, and J. Wakil, "Spatially resolved imaging of microprocessor power : Hotspots in microprocessor," *IEEE Thermal and Thermomechanical Phenomena in Electronics systems Confrence*, May 2006.
- [32] H. F. Hamann, "Method and system for measuring temperature and power distribution of a device ," *United States Patent*, US71767806 B2, Jan. 2007.
- [33] R. Grims and M. Davies, "Optical measurement of an electronic system air flow and temperature distribution," *Journal of optics-Pure and Applied Optics*, March 2004.
- [34] F. J. Mesa, M. Brown, and J. Nayfach, "Measuring performance , power and temperature from real processor," *IEEE International Symposium on Parallel and Distributed Processing* , pp. 1-5, April 2008.
- [35] S. Lee, "*How to select a heatsink*," Director Advanced Thermal Engineering Aavid Thermal Technologies, Inc. Laconia, New Hampshire, 1994.

- [36] OMEGA Company, Digital thermometer data sheet, [Online document], June 2009, Available at http://www.omega.ca/shop/pptsc.asp?ref=HH-20SW_21A_22A_23A&flag=1.
- [37] Intel Pentium® Dual-Core Desktop Processor E2000 Series Datasheet, [Online document], March2008, Available at <http://download.intel.com/design/processor/datasheet/316981.pdf>.
- [38] Intel Pentium® Dual-Core Desktop Processor E2000 Series Datasheet, [Online document], March2008, Available at <http://download.intel.com/design/processor/datasheet>.
- [39] F. P. Incropera and D. P. DeWitt, *Fundamental of Heat transfer*, 4th Edition, John Eiley and sons, 1996.
- [40] E. Sartori, "Convection coefficient equations for forced air flow over flat surfaces," *International journal of Solar Energy*, vol.80, pp 1063–1071, 2006.
- [41] B. Arindam and A. Malcolm, "A convection heat transfer correlation for a binary air-helium mixture at low Reynolds number," *Journal of heat transfer*, vol.129, no. 11, pp. 1494-1505, 2007.
- [42] Y. Xuan and Q .Li, "Investigation on convective heat transfer and flow features of nanofluids," *Journal of heat transfer*, vol. 125, Feb. 2003.
- [43] Intel LGA775 Mechanical design guide, [Online document], Feb. 2006, Available at <http://www.intel.com/Assets/PDF/designguide/302666.pdf>.
- [44] Y. Shabany, "Component size and effective thermal conductivity of printed circuit boards," Applied Thermal Technologies, LLC, [Online document], June 1992, Available at <http://www.thermalcooling.com/reference/thermal-design-reference.shtml>.
- [45] COMSOL Inc., "COMSOL Documentation, Modeling Guide" Burlington MA01803, 2005.
- [46] SPEC CPU2006 Benchmark Descriptions, [Online document], 2008, Available at <http://www.spec.org/cpu2006>.

- [47] Pspice student version, Release 9.1, March 2009, www.orcad.com.
- [48] FDD8780/FDU8780 N-Channel PowerTrench® MOSFET 25V, 35A,[Online document], Aug. 2009 , Available at www.fairchildsemi.com
- [49] Y. Cheng and Ch. Hu, *MOSFET modeling and BSIM3 user's guid*, University of California, Berkeley, 2000.
- [50] Y. Cheng and Ch. Hu., *BSIM3 Manual (version 2.0)*, University of California, Berkeley, March 1994.
- [51] FLIR Company, "Thermovision® SC4000/SC6000 User's guide," No.420-0044-00-10, Version 210, April 2008.
- [52] Flir System, "APACHE SDK documentation," No.110-0114-03, Version 1.10.0, April 2008.
- [53] S. Wanggen, Z. Yiki, W. Xianghua, and J. Zhao, "Design of an ultra-low-power digital processor for passive UHF RFID tags," *IEEE Journal of Semiconductors*, vol. 30, no. 4, 2009.
- [54] N. Arora, *MOSFET modeling for VLSI simulation, Theory and practice*, World Scientific Publishing Co., Inc. River Edge, NJ, USA, 2007.
- [55] W. Huang and E. Skadron, "The need for a full-chip and package thermal model for thermally optimized IC designs," *IEEE International Symposium on Low Power Electronics and Design*, pp. 173-178, 2005.
- [56] G. Digele, S. Lindenkreuz, and E. Kasper, "Fully coupled dynamic electrothermal simulation," *IEEE Transaction VLSI system*, vol. 5, pp. 250-257, SEP 97.
- [57] R. Gonzalez and B. M. Gordon, "Supply and threshold voltage scaling for low power CMOS," *IEEE Journal of Solid-State Circuits*, vol. 32, no. 8, 1997.

- [58] H. F. Hamann and J. Lacey, "Spatially-resolved imaging of microprocessor power (SIMP): hotspots in microprocessors," *Thermal and Thermomechanical Phenomena in Electronics Systems, IEEE Computer Society*, pp. 121–125, May 2006.
- [59] C. Isci and M. Martonosi, "Runtime power monitoring in high-end processors: Methodology and empirical data," *Proceedings of the 36th annual IEEE/ACM International Symposium on Microarchitecture*, pp. 93-104, 2003.

Publications

- 1- F. A. Mohammadi, F. Farrokhi, and M.C.E. Yagoub “Advanced thermal imaging and measurement techniques: Application to a printed circuit board,” *Accepted for the publication at the International Journal of Design, Analysis and Tools for Integrated Circuits and Systems(JDATICS).*
- 2- F. Farrokhi and F. A. Mohammadi “A new approach for electrothermal analysis of integrated circuits, “*To be submitted to the IEEE International Symposium on Circuits and Systems (ISCAS 2010), May 30-June02, 2010, Paris, France.*